

## Reconstruction of Tidal Discharges in the St. Lawrence Fluvial Estuary: The Method of Cubature Revisited

Pascal Matte<sup>1</sup>, Yves Secretan<sup>2</sup>, and Jean Morin<sup>3</sup>

<sup>1</sup> Meteorological Research Division, Environment and Climate Change Canada, 801 - 1550, avenue d'Estimauville, Québec, Québec, G1J 0C3, Canada.

<sup>2</sup> Centre Eau Terre Environnement, Institut National de la Recherche Scientifique, 490, rue de la Couronne, Québec, Québec, G1K 9A9, Canada.

<sup>3</sup> National Hydrological Service, Environment and Climate Change Canada, 801 - 1550, avenue d'Estimauville, Québec, Québec, G1J 0C3, Canada.

Corresponding author: Pascal Matte ([pascal.matte@canada.ca](mailto:pascal.matte@canada.ca))

### Key Points:

- Tidal discharges are computed by integration of the continuity equation, based on known water levels, upriver inflows and river geometry
- Improvements include the use of temporally and spatially continuous nonstationary tidal data and computation of time-varying wetted areas
- Mean error ratios of modeled to observed tidal flows amount to 4.5 % of the tidal discharge amplitudes in the St. Lawrence fluvial estuary

This article has been accepted for publication and undergone full peer review but has not been through the copyediting, typesetting, pagination and proofreading process which may lead to differences between this version and the Version of Record. Please cite this article as doi: 10.1029/2018JC013834

© 2018 American Geophysical Union

Received: Jan 26, 2018; Revised: May 05, 2018; Accepted: May 09, 2018

## Abstract

Knowledge of tidal flows in rivers and estuaries is often scarce yet vital in determining flushing properties and sediment transport rates. While many rivers still remain ungauged, methodological difficulties often arise in gauged systems, resulting in short flow records compared to historical water level data. Notwithstanding, discharge reconstructions in estuaries are possible using indirect methods based on long-term tidal data. In this paper, we revisit the method of cubature, integrating the continuity equation for discharges at different sections. The method consists in computing temporal changes in water volume from simultaneous tidal heights readings along the river and storage width estimations. These water balance estimates remain challenging to produce, because they require spatial interpolation of gappy tidal records and an accurate representation of inundated areas over time. Improvements on the method are made by using a 1D nonstationary tidal harmonic model that provides continuous tidal data along the estuary, with no temporal or spatial gaps. Secondly, a 2D finite element discretization is used to compute the time-varying wetted surface area, relying on detailed topographic data over intertidal flats. The method is applied to the St. Lawrence fluvial estuary (SLFE) and validated against discharge data collected along 9 cross-sections of the river, reaching relative RMSE below 4% of the diurnal tidal discharge range at downstream locations and below 9 % upstream. One-year reconstructions conducted in the SLFE also show the potential of the method to reproduce the tidal discharge variability along the tidal-river continuum, for a wide range of temporal scales.

## 1 Introduction

Many dynamical processes in tidal rivers and estuaries depend on the tidal and tidally-averaged (residual) flow patterns. For instance, concentrations in suspended sediment, and particularly the position of the turbidity maximum, vary seasonally as a function of the freshwater discharge (*Fettweis et al.*, 1998). Sediment fluxes also vary with the tidal phase over the neap-spring cycle depending on the duration and strength of ebb and flood tidal flows (*Castaing and Allen*, 1981; *Kitheka et al.*, 2005; *Prandle*, 2004). Similarly, intratidal, fortnightly and seasonal variations in mixing, stratification and secondary circulation can be observed in many estuaries, which can be linked to tidal asymmetry, the modulation of tidal current amplitudes over the neap-spring cycle and seasonal freshwater inputs to the system (*Chant*, 2002; *Hasan et al.*, 2013; *Jay and Smith*, 1990; *Li and Zhong*, 2009; *Simons et al.*, 2010; *J H Simpson et al.*, 1990). These processes govern biological productivity, for example by concentrating consumer biomass and production (*Simenstad et al.*, 1990). They also influence pollutant dissemination and, more generally, estuarine ecology and morphology (*Prandle*, 2009).

Discharge estimates to the ocean are an important part of land/ocean exchange (*Syvitski et al.*, 2005). Accurate discharge estimations are needed for dynamical inquiries, but also for coastal protection and navigation purposes, as they influence both subtidal water levels (*Buschman et al.*, 2009) and tidal amplitudes (*Godin*, 1985). Moreover, historical analyses over periods from seasons to centuries are essential to understand both the short- and long-term effects of climate and anthropogenic changes on sediment flux (*Syvitski et al.*, 2005) and ecosystem dynamics (*Kukulka and Jay*, 2003a; b).

Direct discharge measurements are made using a wide variety of current sensors, one of the most frequently encountered being the acoustic Doppler current profiler (ADCP) (*Muste et al.*, 2004; *Oberg and Mueller*, 2007; *M R Simpson*, 2001). Boat surveys are generally costly,

labor-intensive, unsafe under certain flow or weather conditions, and can rarely be carried out over extended periods. As a result, acquired data are generally used to calibrate empirical relationships between discharge and some other continuously monitored variable, in order to allow real-time estimation of river flow. Traditional empirical approaches to the estimation of unsteady discharges include the method of cubature, the rating-fall method, the tide-correction method, and the coaxial graphical-correlation method (Rantz, 1982). Stage-discharge relationships remain, on the other hand, the most commonly developed rating models in rivers (Aquatic Informatics Inc., 2012). However, they may be prone to high uncertainty, due to temporal changes in channel geometry (e.g., due to erosion and sedimentation) or roughness (e.g., due to vegetation), backwater and nonstationary (e.g., tidal) effects, uncertainty in river flow data and the difficulty of obtaining calibration data during extreme discharge events (Guerrero et al., 2012; Jalbert et al., 2011). These factors limit the use of a single-parameter rating (Di Baldassarre and Montanari, 2009; Le Coz et al., 2008; Nihei and Kimizu, 2008). More advanced unsteady rating curves have been developed to get around this problem, for example using stage measurements at two adjacent cross-sections (Dottori et al., 2009) or neural network models (Hidayat et al., 2014; Supharatid, 2003). However, these models remain subject to uncertainties related to interpolation and extrapolation errors and temporal changes in the relations (Di Baldassarre and Montanari, 2009; Hidayat et al., 2011); in the case of neural network models, they typically lack physical interpretation of the processes in place.

Continuous measurements can alternatively be acquired by vertically- (up-looking) or horizontally- (side-looking) deployed ADCPs (Hidayat et al., 2011; Hoitink et al., 2009; Le Coz et al., 2008; Levesque and Oberg, 2012; Nihei and Kimizu, 2008; Ruhl and Simpson, 2005). In these cases, discharge may be inferred based on the index velocity method (Chen et al., 2012; Healy and Hicks, 2004; Ruhl and Simpson, 2005), the velocity profile method (Le Coz et al., 2008), or a combination of the two (Hoitink et al., 2009; Sassi et al., 2011). Non-contact methods, such as large-scale particle image velocimetry (Daigle et al., 2013; Muste et al., 2008) and radar wave scattering (Costa et al., 2006), also provide new means for surface velocity and flow measurements. Similarly, remotely sensed hydraulic data and river features have been used to infer flow characteristics (Bjerklie et al., 2005; Durand et al., 2014; Grünler et al., 2013; Pavelsky, 2014; Plant et al., 2009). Although very attractive, long-term deployments are sometimes impractical (e.g., in a navigation channel or in presence of a mobile bed) and the frequency of acquisition of remotely sensed observations may be too low compared to the variability of the measured flows, especially in tidal environments. Conversely, numerical modeling may be laborious and is generally not setup for long-term analyses.

As a result, the length of flow records in rivers and estuaries tends to be much shorter than historical time series of water levels. Moreover, discharge gauging stations are usually limited in number and most often located above the head of the tide. In this latter case, any tributary inflows or water losses occurring seaward of the station remains unmeasured, which can represent a considerable amount of water in wet coastal regions, particularly during floods. This calls for the development of new indirect methods for the reconstruction of historical discharge time series within tidal estuaries based on available long-term data, such as water levels.

An inverse model, developed by Jay and Kukulka (2003) and revised by Mofstakhari et al. (2013) to include a quantification of uncertainties, was used to hindcast freshwater discharge from wavelet and harmonic analyses of tidal properties in the Columbia River and San Francisco

Bay, respectively. This model was updated using a multiple-gauge approach and applied to the Columbia and Fraser River estuaries, improving the temporal resolution of the discharge estimates by accounting for neap-spring storage effects (*Moftakhari et al.*, 2016). In contrast, *Cai et al.* (2014) developed an inverse analytical, rather than statistical, approach for estimating freshwater discharge on the basis of tidal water level observations along the Yangtze estuary, more specifically relating tidal damping and tidally-averaged depth (including residual water level) to river flow. While these authors focused on reconstructing historical, tidally-averaged (residual) flows in estuaries, our attention here is directed towards the unsteady (tidal) part of this flux and its longitudinal variability within a tidal river.

In this paper, we revisit the method of cubature (*Dronkers*, 1964; *Pillsbury*, 1939), one of the oldest methods of computing discharges in tidal rivers and estuaries. The method consists in integrating the continuity equation for discharges at different sections, using simultaneous tidal heights readings at stations distributed along the river. Temporal changes in water volume are computed between each section and the head of the tide, based on interpolated water levels and river storage widths. Discharge time series are obtained by subtracting the computed time-varying volumes from measured (or estimated) upland and tributary inflows at the upstream and lateral boundaries.

Applications of the method of cubature for the estimation of volume fluxes can be found, for example, in Mobile Bay (*Dzwonkowski et al.*, 2015), the Chesapeake Bay (*Xiong and Berger*, 2010), the Ria de Aveiro estuary-coastal lagoon system (*da Silva and Duck*, 2001), the Conwy estuary (*Wallis and Knight*, 1984), the Scheldt estuary (*Dierckx et al.*, 1981) and the St. Lawrence River (*Forrester*, 1972). Various techniques have been employed to spatially integrate tidal heights and storage widths. For example, in the St. Lawrence River, *Forrester* (1972) used a simple partitioning of the river geometry into regions of constant surface area (taken at mean water level), scaled from Canadian Hydrographic Service (CHS) charts, with harmonic constituents from one or more tide gauges taken to represent each region. In the Conwy estuary, *Wallis and Knight* (1984) used smoothed linear interpolations of tidal heights and measured section profiles to reconstruct tidal discharges. Similarly, *da Silva and Duck* (2001) used linear interpolation of water levels and gridded bathymetry to compute the water volumes in the Ria de Aveiro at a given time. In contrast, *Dierckx et al.* (1981) derived tidal discharge estimates in the Scheldt estuary based on two-dimensional smoothing spline approximations of the water level and storage width, expressed as functions of longitudinal position and time.

These water balance estimates remain challenging to produce, because they require spatial interpolation of (sometimes gappy) tidal records and an accurate representation of inundated areas over time. One way to get around the problem of data gaps is to replace measured water levels by a harmonic representation of the tides, fitted to the data. Such a model offers the possibility to predict water levels, expressed as a sum of sinusoids from which time-invariant constituent amplitudes and phases can be retrieved. While this approach has been pursued by some authors (*da Silva and Duck*, 2001; *Forrester*, 1972), no previous cubature studies have considered the nonstationary and nonlinear behaviour of river tides under which, for example, tides are being damped by river flow (*Guo et al.*, 2015). Under these conditions, classical harmonic analysis fails to represent the total variability of water levels (*Matte et al.*, 2014b); therefore, it cannot be effectively used to fill temporal gaps in nonstationary tidal records. Spatial interpolation of tidal records is another issue in conventional cubature methods. Most techniques apply linear or spline interpolators to water level data in order to obtain a

spatially continuous representation of the water levels throughout the domain (*da Silva and Duck, 2001; Dierckx et al., 1981; Wallis and Knight, 1984*). Spatial interpolation of tidal constituents, on the other hand, allows the information on tidal properties (i.e. amplitudes and phases) to be transferred to the flow estimations and the contribution of each tidal constituent to the total tidal discharges (and section-averaged tidal currents) can be deduced (*Forrester, 1972*). With nonstationary tides, however, tidal constituent interpolation is not a trivial task (*Matte et al., 2014b*) and has never been applied to cubature reconstructions before, to the authors' knowledge. Lastly, shortcomings of the cubature method can often be seen in the way that storage widths are accounted for. Constant surface areas are not desirable if the superficies of intertidal flats are substantial. Moreover, measured section profiles ought to be replaced by complete bathymetric and topographic dataset, especially over shallow areas, for accurate time-varying volume estimations (*da Silva and Duck, 2001*), although this is not yet common practice.

A new adaptation of the method of cubature is presented here in order to address the shortcomings of previous implementations, with respect to (1) the interpolation of nonstationary tidal records with temporal and spatial gaps, and (2) the computation of time-varying wetted areas. Improvements on the method include the use of a 1D nonstationary tidal harmonic model (*Matte et al., 2013; Matte et al., 2014b*), specifically adapted to the nonstationary tidal context, that provides temporally and spatially continuous predictions in place of discrete (measured) tidal data along the estuary, with no temporal or spatial gaps. This model spatially integrates tidal heights by reconstruction of the interpolated tidal coefficients between the stations, thus carrying information about the physics, as opposed to conventional interpolators. Secondly, a 2D finite element discretization is used to compute the time-varying wetted surface areas and discharges, relying on predicted water levels (expanded laterally from the 1D longitudinal profiles of tidal heights) and a detailed digital elevation model (DEM) over the domain, composed of high-resolution river topography over intertidal flats and shoals.

The method is applied to the St. Lawrence fluvial estuary (SLFE), a 180-km freshwater stretch of the St. Lawrence River characterized by strong tidal and river flows. Several tributaries enter this reach of the SLFE, some of which contributing significantly to the total river discharge during floods. While water level records are available at numerous stations in the SLFE, some dating back to the late 19<sup>th</sup> or early 20<sup>th</sup> centuries, discharge data are very scarce. Previous flow velocity and discharge measurement campaigns in the SLFE are documented by *Dohler (1961), Godin (1971), Prandle (1971), Prandle and Crookshank (1972), Long et al. (1980), and Bourgault and Koutitonsky (1999)*. Due to the resolution and length of these records (from 1 day to 1 month), only limited insight has been gained into the spatial and temporal variability of the tidal flows. Seasonal and interannual variability, and trends, have not been looked at before. More recently, detailed cross-sectional water level and velocity data were collected along 13 transects of the SLFE, each repeatedly surveyed during one tidal cycle, providing the first comprehensive field description of the tidal hydrodynamics of this largely undocumented region (*Matte et al., 2014a*). This data set is used herein to validate the discharge time series reconstructed by cubature.

This paper aims at characterizing the longitudinal and temporal variability (from intratidal to seasonal) of tidal discharges in the SLFE. It elaborates on the development and validation of this new implementation of the method of cubature, which is then applied to the analysis of a one-year hydrograph characterized by a wide range of river flows. This paper is divided as follows. The methods are presented in section 2, followed by application of the model

to the SLFE in section 3. Validation results and analysis of one-year tidal discharge reconstructions are provided in section 4, along with an error analysis and general discussion on benefits and limitations of the method. Concluding remarks are given in section 5. Appendix A presents the procedure used to derive observed discharges from water level and velocity data in the SLFE. Appendix B presents a derivation of the 1D tidal harmonic model used for interpolation, including its underlying assumptions and approximations, also described in *Matte et al.* (2014b). Appendix C details the finite element approximation used to integrate the continuity equation. Results for the entire set of validation transects are provided in an electronic appendix.

## 2 Methods

### 2.1 Method of Cubature

The method of cubature consists in computing the time-varying discharge at a river cross-section through integration of the continuity equation, based on the knowledge of water levels, upland and tributary inflows and river geometry. Mathematically, the continuity equation in its integral form can be expressed as:

$$\int_{\Omega} \vec{\nabla} \cdot \vec{q} d\Omega = - \int_{\Omega} \frac{\partial h}{\partial t} d\Omega, \quad (1)$$

where  $q$  is the specific discharge ( $\text{m}^2 \text{s}^{-1}$ ),  $h$  is the water level (m),  $t$  is time (s) and  $\Omega$  is the surface area ( $\text{m}^2$ ). Applying the divergence theorem to the left-hand side of Eq. (1) yields a contour integral along  $\Gamma$ :

$$\oint_{\Gamma} \vec{q} \cdot \vec{n} d\Gamma = - \int_{\Omega} \frac{\partial h}{\partial t} d\Omega. \quad (2)$$

With a control volume defined along the river margins, the contour integral equals the sum of inflows and outflows  $Q_i$  through the system boundaries:

$$\sum_i Q_i = - \int_{\Omega} \frac{\partial h}{\partial t} d\Omega. \quad (3)$$

The inflows and outflows  $Q_i$  can further be divided into the known upstream and tributary discharges,  $Q_r$ , and the unknown (calculated) discharges at the downstream boundary,  $Q_{tot}$ :

$$\sum_i Q_i = Q_{tot} - \sum_r Q_r. \quad (4)$$

The final form of the equation, relating the downstream discharge to the upstream river discharge and water storage per unit time, is given as:

$$Q_{tot} = \sum_r Q_r - \int_{\Omega} \frac{\partial h}{\partial t} d\Omega. \quad (5)$$

The tidal discharge (i.e. discharge variations due to the tides) is approximated by the integral on the right-hand side of Eq. (5). Section-averaged tidal currents can be obtained by dividing the tidal discharge by the time-varying cross-sectional area.

## 2.2 1D Nonstationary Tidal Harmonic Model

The water levels  $h$  and their time derivatives  $\frac{\partial h}{\partial t}$  appearing in Eq. (5) are derived from a 1D nonstationary tidal harmonic model, developed by *Matte et al.* (2014b). The model derivation and underlying assumptions are summarized in Appendix B. Use of a 1D tidal harmonic model allows interpolation of stage and tidal constituent properties between stations at any location ( $r$ ) along the river at any given time ( $t$ ). Longitudinal profiles of the water levels  $h$  are given as:

$$h(r, t) = s(r, t) + f(r, t), \quad (6a)$$

with:

$$s(r, t) = c_0(r) + c_1(r)Q_r^{2/3}(t - \tau_Q) + c_2(r)\frac{R^2(t - \tau_R)}{Q_r^{4/3}(t - \tau_Q)}, \quad (6b)$$

$$f(r, t) = \sum_{k=1}^n \left[ \left( d_{0,k}^{(c)}(r) + d_{1,k}^{(c)}(r)Q_r(t - \tau_Q) + d_{2,k}^{(c)}(r)\frac{R^2(t - \tau_R)}{Q_r^{1/2}(t - \tau_Q)} \right) \cos(\sigma_k t) + \left( d_{0,k}^{(s)}(r) + d_{1,k}^{(s)}(r)Q_r(t - \tau_Q) + d_{2,k}^{(s)}(r)\frac{R^2(t - \tau_R)}{Q_r^{1/2}(t - \tau_Q)} \right) \sin(\sigma_k t) \right], \quad (6c)$$

where  $r$  is a curvilinear coordinate following the river thalweg; the superscripts (c) and (s) refer to the cosine and sine terms, respectively;  $c_i$  ( $i = 0, 2$ ) are the model parameters for the stage model  $s(r, t)$ ;  $d_{i,k}$  ( $i = 0, 2$ ) are the model parameters for the tidal-fluvial model  $f(r, t)$ ;  $Q_r$  is the upstream river flow ( $\text{m}^3\text{s}^{-1}$ );  $R$  is the greater diurnal ocean tidal range (m);  $\sigma_k$  are a priori known frequencies;  $k$  is the index for  $n$  tidal constituents ( $k = 1, n$ );  $\tau_Q$  and  $\tau_R$  are the time lags applied to the  $Q_r$  and  $R$  time series, respectively, representing the average time of propagation of the waves to the analysis stations (cf. *Matte et al.*, 2014b). The stage model  $s(r, t)$  represents low-frequency variations of the mean water level (MWL) associated with the influence of river discharge and ocean tidal range. The tidal-fluvial model  $f(r, t)$ , for its part, expresses the variability of tidal constituent amplitudes and phases in terms of the same external forcing variables (cf. Eq. (B8a-b)).

The time derivatives  $\frac{\partial h}{\partial t}$  evaluated at time  $t_j$  are calculated from Eq. (6) and approximated by:

$$\frac{\partial h(r, t_j)}{\partial t} = \frac{\partial s(r, t_j)}{\partial t} + \frac{\partial f(r, t_j)}{\partial t}, \quad (7a)$$

with:

$$\frac{\partial s(r, t_j)}{\partial t} \approx \frac{s(r, t_{j+1}) - s(r, t_{j-1})}{t_{j+1} - t_{j-1}}, \quad (7b)$$

$$\frac{\partial f(r, t_j)}{\partial t} \approx \sum_{k=1}^n \frac{f_k(r, t_{j+1}) - f_k(r, t_{j-1})}{t_{j+1} - t_{j-1}}. \quad (7c)$$

For the stage model (Eq. (7b)), time derivatives are calculated using centered finite differences, rather than by taking the derivative of Eq. (6b), which would require computing finite differences separately on  $\frac{\partial Q_r}{\partial t}$  and  $\frac{\partial R}{\partial t}$ . Similarly, for the tidal-fluvial model (Eq. (7c)), time derivatives are calculated using centered finite differences, separately for each tidal constituent  $k$ .

### 2.3 2D Finite Element Discretization

To accurately compute the time-varying wetted surface area and discharges, the integration surface  $\Omega$  in Eq. (5) is represented by a 2D mesh with a simple wetting-drying algorithm. The solution to the integral on the right-hand side of Eq. (5) is obtained based on a 2D finite element approximation to the continuity equation, detailed in Appendix C. The solution is computed over a discretized domain composed of three-node triangular elements (T3), with nodal values  $\frac{\partial h_n}{\partial t}$  corresponding to the time derivative of  $h$ .

The nodal values  $\frac{\partial h_n}{\partial t}$  are derived from the 1D longitudinal profiles  $\frac{\partial h(r,t)}{\partial t}$  (cf. Eq. (7)) as follows: for each node of the 2D grid, the closest point along the 1D curvilinear path  $r$  is identified, in terms of the minimum Euclidean distance, and the corresponding value of  $\frac{\partial h(r,t)}{\partial t}$  is assigned to the node. In other words, the longitudinal profiles of tidal heights and their time derivatives, given by the 1D tidal harmonic model, are expanded laterally and projected on the 2D finite element mesh, assuming no lateral slopes. The actual water level distribution, however, naturally presents lateral gradients influenced by channel curvature, bathymetry and the presence and extent of intertidal flats. These gradients can be associated with amplitude differences and phase lags of the tide between the deeper channel and the off-channel shallow areas. For example, tidal ranges in the SLFE are larger in the channel than on the tidal flats. Similarly, high water (HW) and low water (LW) timings are found to occur later over shallow topography than in deeper parts of the river channel, with larger time lags for LW than HW responsible for increased tidal asymmetry (Matte *et al.*, 2017b). In contrast, tidal monthly variability in the floodplain may be stronger than or quite different from nearby channel locations (Jay *et al.*, 2015) Despite this simplification, making such an assumption removes the need for numerically solving the 2D momentum equation, by instead extrapolating the water levels from predetermined longitudinal profiles, which leaves us with integrating only the continuity equation for discharges (with no friction parameterization).

The integration domain  $\Omega$  in Eq. (5) corresponds to the wetted surface area, which varies in time as a function of the tide and river discharge. A wetting-drying condition is therefore added to the computation in order for the mass to be conserved, where dry nodes (i.e. nodes for which the water level is lower than the topography) are assigned null values of  $\frac{\partial h_n}{\partial t}$ , or, equivalently, time-invariant water levels equal to the bed elevation. To allow this comparison between water levels and bed elevation to be performed on the grid nodes, topographic data are also interpolated on the 2D mesh.

Solution to the integral in Eq. (5) over  $\Omega$  is given by the sum of all elemental discharges,  $Q^e$ , yielding:

$$Q_{tot} = \sum_r Q_r - \sum_e Q^e, \quad (8)$$

where  $Q^e$  is computed as the average of the nodal values composing the T3 element multiplied by the elemental surface area (cf. Appendix C).

## 2.4 Error Estimation

To evaluate the error made on the computed discharges in Eq. (8), a simple estimate of the uncertainty in  $Q_{tot}$  is used, denoted  $\delta Q_{tot}$ :

$$\delta Q_{tot} = \sqrt{\sum_r (\delta Q_r)^2 + \left| \sum_e Q^e \right|^2 \left[ \left( \frac{\delta R}{R} \right)^2 + \left( \frac{\delta \Omega}{\Omega} \right)^2 \right]}. \quad (9)$$

The first term on the right-hand side of Eq. (9) corresponds to errors in the input upstream and tributary discharges. The second member on the right-hand side is composed of two terms representing the uncertainty on the integral appearing in Eq. (5), whose solution is given by the sum of elemental discharges, or  $\sum_e Q^e$  (cf. Eq. (8)). First, the error on the time derivative of  $h$  from Eq. (5) is approximated by the uncertainty in tidal range  $\delta R$ , which is taken here to represent random errors in tidal heights. Second, systematic errors in water levels and topography, in contrast, have no effect on the time derivative of  $h$ , but affect, in turn, the superficies of wetted areas; thus they are accounted for through the uncertainty in the wetted surface area  $\delta \Omega$ . The relative errors for  $R$  and  $\Omega$  are multiplied in Eq. (9) by the amplitude over a tidal cycle of the summed elemental discharges, yielding tidally-averaged estimates of the error in tidal discharge.

## 3 Application to the SLFE

### 3.1 Setting

The St. Lawrence River is the third largest river in North America. It connects the Great Lakes with the Atlantic Ocean and is the primary drainage of the Great Lakes basin, one of the most industrialized regions of the world. The average freshwater discharge is  $12\,200 \text{ m}^3\text{s}^{-1}$  at Québec, but historical minimum and maximum daily net discharges respectively amounted to  $7\,000 \text{ m}^3\text{s}^{-1}$  (March 1965) and  $32\,700 \text{ m}^3\text{s}^{-1}$  (April 1976) over the 1960–2010 period, taking into account the contribution of all tributaries and drainage areas upstream of Québec (*Bouchard and Morin, 2000*). The effects of such variations on MWLs and tidal range are severe, particularly in the upper portion of the SLFE (*Godin, 1999; Matte et al., 2014b*).

The SLFE spans 180 river kilometers (rkm) from the exit of Lake Saint-Pierre to the eastern tip of Orleans Island, located at the upper limit of saline intrusion (Figure 1). The circulation of the SLFE is characterized by vertically well-mixed freshwater and driven by strong tidal and river flows. Ocean tides are amplified as they enter the St. Lawrence until they reach their highest level ( $\sim 7 \text{ m}$  in range during the largest spring tides) in the upper estuary at Saint-Joseph-de-la-Rive – hereafter referred to as rkm 0. Increases in water levels of more than  $1 \text{ m h}^{-1}$

can be observed during the rising tide, leading to rapid changes in flow conditions as well as in the wetted areas. This generates strong current reversals with peak tidal discharges up to five times larger than the daily average in both the upstream and downstream directions. The tidal signal is increasingly distorted and damped as it propagates upstream due to nonstationary and nonlinear effects associated with fluctuating river flow and frictional effects. As a result, longitudinal variations in the dynamical regime occur, characterized by marked changes in the water level slopes. Following these breaks, the SLFE can be divided into four contrasting reaches (*Matte et al.*, 2014b): (i) a tide-dominated region downstream of Portneuf (rkm 163.5); (ii) a transition zone from the tidal to the tidal-fluvial regimes between Portneuf and Cap-à-la-Roche (rkm 186), characterized by a rapid increase in bottom slope; (iii) a tidal-fluvial reach between Cap-à-la-Roche and the Laviolette Bridge (rkm 235), the latter acting as a major restriction to the flow; and (iv) an upstream fluvial reach landward of Lake Saint-Pierre where the semidiurnal tide gradually extinguishes, but with fortnightly modulations of the MWL persisting as far as Montreal (rkm 360). The limit where the flow becomes unidirectional (i.e. only one slack water) moves as a function of tidal range and river discharge, between zones (i) and (iii).

## 3.2 Data

### 3.2.1 Tide Data

Tide data used in the cubature calculations were taken from a mix of permanent and temporary tide gauges maintained by Canada's Department of Fisheries and Oceans (DFO), along with pressure sensors installed from May to October 2009 in the SLFE (Figure 1) (*Matte et al.*, 2014a). These data form the basis of the 1D tidal harmonic model used for the interpolation of tidal heights (cf. section 2.2) (*Matte et al.*, 2014b). Data are vertically referenced to the mean sea level (MSL).

### 3.2.2 Discharge Data

Daily net discharge data in the St. Lawrence River are based on a stage-discharge relationship at the station of Lasalle, located above the head of the tide (Figure 1). Downstream, these estimates are progressively modified to account for flows from tributaries. These inflows are, for the most part, reconstructed from stage-discharge relationships established by the Government of Québec (Direction de l'Expertise Hydrique, Ministère du Développement durable, de l'Environnement et de la Lutte contre les changements climatiques; <https://www.cehq.gouv.qc.ca/>) or by Hydro-Québec. For each tributary, the discharge measured at an upstream station is multiplied by a factor specific to each river, based on drainage areas, to include the estimated lateral inflow coming from the basin downstream of the gauge (assuming hydrological homogeneity within the basins). For ungauged areas, the inflow is estimated from the runoff coefficient of an adjoining gauged area. Relations for each tributary to the St. Lawrence were developed by *Morse* (1990) and updated by *Bouchard and Morin* (2000). A recent validation of *Morse's* calculated drainage areas pointed out a few inaccuracies in his calculations (*Boudreau and Fortin*, 2018). First, the watershed areas were underestimated by about 7% by *Morse* (1990) on average. Furthermore, during high discharge events, discrepancies of the order of  $1000 \text{ m}^3\text{s}^{-1}$  in cumulative discharges to the St. Lawrence River at Trois-Rivières were observed between *Morse's* calculation and the corrected estimates, using the year 2012 as a reference. Under average conditions, however, *Morse's* formulas only underestimated the discharge in the St. Lawrence River by  $100 \text{ m}^3/\text{s}$ . Comparisons between *Morse's* calculations and

the updated formulas was not performed for tributaries downstream of Trois-Rivières, but discrepancies are expected to be relatively low for all tributaries but the Chaudière River (located by the Quebec Bridge; Figure 1), where peak discharges may be considerable ( $\sim 1000 \text{ m}^3/\text{s}$ ). A similar, though possibly more complete, approach is followed by the California Department of Water Resources in the San Francisco Bay delta to estimate a Net Delta Outflow Index (NDOI). The NDOI accounts for tributary inflows, net agricultural water demands, and surface runoff from precipitation (California Department of Water Resources, 2016). A full hydrological model (Durnford *et al.*, 2017) or the inverse models developed by Jay and Kukulka (2003) or Cai *et al.* (2014) could alternatively be used to reconstruct residual flow and validate these estimates, although this was not done here.

To date, no tidal discharge data have been routinely collected in the SLFE, from either direct measurements or indirect methods. The method of cubature presented here (cf. section 2.1) is therefore used to reconstruct historical discharge time series at a series of cross-sections in the SLFE. These estimates are validated using discharge observations derived from water level and velocity data collected along the same transects, each surveyed over approximately one tidal cycle during a field campaign conducted in the summer of 2009, described in detail in Matte *et al.* (2014a). The authors devised a procedure to reconstruct continuous and synoptic water level and velocity fields from non-synoptic real-time kinematic global positioning system (RTK GPS) and ADCP measurements, respectively. From these fields, computation of the time-varying discharges was carried out following a procedure detailed in Appendix A.

A first-order approximation of the relative errors in observed discharge is provided in Table 1 at 13 measurement transects in the SLFE. Errors in cross-sectional area are neglected in the calculation, assuming that they are one order of magnitude smaller than errors in velocity. The latter are dominated by smoothing and interpolation errors, whose values are provided in Matte *et al.* (2014a).

### 3.2.3 Topographic Data

A DEM is used to compute the wetted area at each time step of the cubature calculation. Topographic data includes channel bathymetry, floodplains, and engineering structures. Bathymetric data were obtained from the CHS and consist of a mix of high-resolution multibeam echosoundings in the navigational channel and lower-resolution (older) data outside the channel or in shallower areas. To complete the topography in the floodplains, marshes, shoals and intertidal zones, data from LIDAR campaigns conducted during the fall of 2001 and summer of 2012 were used (Matte *et al.*, 2017a; Morin and Champoux, 2006).

Major tributaries were included in the model to allow water to be cyclically stored and evacuated as a function of the tide. Their boundaries were positioned at upstream locations removed from tidal influence. The geometry of the river shores was extracted using geospatial data from Natural Resources Canada's GeoBase website (<http://www.geobase.ca/>). Their bathymetry was represented, due to a lack of data, by a regularly shaped trapezoidal channel of constant slope and variable depth and width. Channel depth was determined by calculating the depth needed to discharge the average river flow at an approximate mean velocity of  $1 \text{ m s}^{-1}$ , given the local width of the river. Finally, engineering structures, such as bridge pillars, piers, marinas and ports, were also included as topographic elements.

### 3.3 Model Properties

#### 3.3.1 Harmonic Analyses and Interpolation

In order to build the 1D spatial model, nonstationary tidal harmonic analyses were performed using NS\_TIDE (Matte *et al.*, 2013) on hourly water level data from 13 tide gauges distributed between Saint-Joseph-de-la-Rive and Lanoraie (Table 2), over the 1999–2009 period. The tidal-fluvial model (cf. Eq. (6)) was forced using 39 tidal components, listed in Table 3. The same constituents were included at all stations to allow spatial interpolation of model coefficients throughout the system. Iteratively reweighted least-squares (IRLS) analyses (cf. Eq. (B3)) were performed using a Cauchy weighting function with a default tuning constant of 2.385 (Leffler and Jay, 2009). Spatial interpolation of model coefficients was carried out between the analysis stations using piecewise cubic Hermite interpolants (Fritsch and Carlson, 1980), which are continuous up to the first derivatives and preserve monotonicity. The remaining intermediate stations appearing in Figure 1 (shown in italics in Table 2) were used for validation of the interpolated water levels (cf. Matte *et al.*, 2014b). The overall prediction accuracy of the 1D tidal harmonic model is better than 30 cm in water levels at all stations (Matte *et al.*, 2014b).

The discharge time series  $Q_r$  (cf. Eq. (4)) used in the analyses are reconstructed by the method of Bouchard and Morin (2000) (cf. section 3.2.2); they are presented in Matte *et al.* (2014b). A one-year sample (August 2007 – August 2008) of the time series is provided in Figure 2 (top panel). Differences in discharge between Trois-Rivières and Québec reached a maximum of  $8700 \text{ m}^3\text{s}^{-1}$  in April 2008 during the freshet, due to the contribution of lateral inflows from tributaries. Minimum and maximum discharges at Québec for the 1999–2009 period were observed in September 2007 ( $7600 \text{ m}^3\text{s}^{-1}$ ) and April 2008 ( $26\,400 \text{ m}^3\text{s}^{-1}$ ), respectively. Historical extreme flows occurred in March 1965 ( $7000 \text{ m}^3\text{s}^{-1}$ ) and April 1976 ( $32\,700 \text{ m}^3\text{s}^{-1}$ ) for the 1960–2010 period. Therefore, the chosen 11-year analysis period represents most of the variability in the modern system.

The station of Sept-Îles, removed from fluvial influence, was used as the reference station for ocean tidal forcing (Figure 1) (cf. Matte *et al.*, 2014b). Daily greater diurnal tidal ranges  $R$  were extracted from hourly data at the station. Water levels were high-pass filtered, then re-interpolated using cubic spline functions to a 6-min interval in order to capture the tidal extrema. Tidal ranges  $R$  were calculated as the difference between higher high water and lower low water using a 27-h moving window with 1-h steps, then smoothed to eliminate discontinuities, similarly to Kukulka and Jay (2003a)'s tidal range filter. A sample of the time series is provided in Figure 2 (bottom panel) for the year 2007–2008. Ocean tidal ranges vary approximately between 1.2 and 3.6 m, and get amplified on their way upstream, before being progressively damped as they enter the fluvial estuary.

Further details on the model setup, performance and validation are provided in Matte *et al.* (2014b).

#### 3.3.2 2D Mesh and Topography

The 2D finite element mesh used for integration covers a section of the St. Lawrence River extending from Québec (rkm 106.5) to Lanoraie (rkm 302), as shown in Figure 3. It is composed of 178 938 nodes and 342 268 T3 elements and has a 67-m average spatial resolution. The DEM associated with this mesh is presented in Figure 4. The reach between Trois-Rivières (rkm 231) and Québec was taken from a high-resolution hydrodynamic model developed by

Matte *et al.* (2017a), whereas the Lake Saint-Pierre region was taken from the Montreal – Trois-Rivières model developed at Environment and Climate Change Canada (Morin and Champoux, 2006). The two grids were respectively truncated at Québec and Lanoraie, and then merged at Trois-Rivières. Discharge variations at the upstream limit are considered as tidally-invariant, although spring-neap oscillations of the MWL are still perceptible at Lanoraie. Amplitude of the semidiurnal tide at this location represents, on average, less than 1% of its amplitude at the SLFE entrance and completely extinguishes during neap tides (Matte *et al.*, 2014b).

For validation with transect data, the mesh was progressively truncated along the surveyed cross-sections (shown in Figure 3), in order to perform each of the discharge reconstructions from the section treated up to the head of the tide.

### 3.3.3 Cubature Analyses

The cubature computations were tested and validated over two periods in June and August 2009, during which the transect data were collected (cf. section 3.2.2). A 6-min time step was used for the input data and discharge computations in order to capture the tidal extrema. Validation of the reconstructed discharges was performed along 9 cross-sections, shown in Figure 3. Statistical goodness of fit criteria were used to assess model performance, including the root-mean-square error (RMSE), the maximum absolute error (MaxAE) and the mean amplitude ratio (MAR) of predicted to observed discharges ( $Q_{pred}$  and  $Q_{obs}$ , respectively), defined as follows:

$$\text{MAR} = \frac{1}{n} \sum_{j=1}^n \frac{Q_{pred,j}}{Q_{obs,j}} \quad (10)$$

The MAR is computed using only values of the absolute instantaneous flow exceeding 20 % of the maximum flow, in order to avoid division by near-zero values, similarly to Lefavre *et al.* (2016). The error associated with the MAR is defined as  $(1 - \text{MAR}) \times 100 \%$ .

In order to illustrate how well the model captures the discharge variability in the SLFE, one-year reconstructions were performed at two contrasting cross-sections: Quebec (rkm 106.5) located in the tide-dominated region and Grondines (rkm 179.5) where tides and MWL are significantly modified by the river discharge. The reconstruction period covers an entire year, extending from August 2007 to August 2008, thus encompassing the tidal range annual variability as well as a wide range of river discharges (cf. Figure 2), from very low flows ( $7600 \text{ m}^3\text{s}^{-1}$ ) to very high flows ( $26\,400 \text{ m}^3\text{s}^{-1}$ ). Two high discharge events occurred in January and April 2008, approximately lasting two weeks and two months, respectively. These flows are fairly extreme when compared to the average discharge of  $12\,200 \text{ m}^3\text{s}^{-1}$  at Québec. The one-year reconstructions were conducted at a 20-min time step.

## 4 Results and Discussion

### 4.1 Validation of the Tidal Discharges

Statistics on the discharge reconstructions made at the validation transects are presented in Table 4. RMSE and MaxAE values cumulate and generally increase from upstream (Trois-Rivières; rkm 231) to downstream (Québec; rkm 106.5), following the increase in extent of the integration domain. However, relative errors (shown in parentheses) tend to decrease as the

variability of tidal discharges gets larger, reaching rRMSE values below 4 % of the diurnal tidal discharge range at downstream locations. Relative errors at upstream locations are less representative of the actual error since tidal discharge amplitude becomes considerably weaker landward (cf. electronic appendix). Nevertheless, rRMSE are lower than 9 % considering all transects but Bécancour and Trois-Rivières, where the length of the discharge records is less than half the tidal period (Table 4). Another measure of the error made is given by the ratio of predicted to observed flows, which represents how well the signal amplitudes are reproduced. Values of the MAR are presented in Table 4 for each transect. Estimated tidal discharge amplitudes fall within 7 % of the observed values at all transects but Portneuf ( $1 - 0.870 = 13.0\%$ ), due to the effects of local channel curvature (see section 4.2.3). Errors associated with the MAR are overall comparable to measurement errors (cf. Table 1); they amount to 4.5 % when averaged over all transects.

Results at the Québec cross-section (rkm 106.5) are presented in Figure 5. On the upper panel are shown the predicted water levels from the 1D tidal harmonic model, which are in good agreement with observations at Québec on June 15, 2009. Variations in the wetted surface area (green dash-dotted curve) illustrate the temporal changes in the entire integration domain, from Québec to Lanoraie. Bottom panel of Figure 5 shows the discharges reconstructed by cubature, compared to transect data acquired over one tidal cycle. Predicted discharges are in good agreement with observations, both in terms of synchronism and amplitude. Slack waters (null discharges) occur slightly after LW and HW at the ebb-to-flood and flood-to-ebb transitions, respectively, indicator of a tidal wave of a mixed character that shares the characteristics of a progressive and a standing wave, typical of alluvial estuaries (*Savenije, 2012*). The duration of the ebb is almost twice that of the flood at Québec, with discharge volumes approximately two times bigger. Considerable freshwater volumes thus exit the estuary periodically.

Validation at the Deschambault cross-section (rkm 168) is shown in Figure 6. Overall, both predicted water levels and discharges at Deschambault are in good agreement with observations. This region encompasses the largest intertidal areas of the SLFE and is characterized by a narrow channel of strong currents at the Richelieu rapids. A sharp decrease in wetted surface area starting a few hours before LW occurs at this section. The shape of both the wetted area and water level differs from the curves at Québec, as the tide gets more and more distorted propagating upstream, due to frictional nonlinearities. Current reversals are still observable at Deschambault, although of shorter duration than at Québec. Flood discharges are also more sensitive to the tidal range, being proportionally more weakened than ebb discharges at lower tidal ranges. This results in a larger daily variability of the ratio of flood to ebb volumes as a consequence of the diurnal inequality of the tide.

Validation results for all cross-sections appearing in Figure 3 are provided in an electronic appendix (Figures S1–S9; from downstream to upstream); they are briefly presented below. At Saint-Nicolas and Neuville (Figures S2–S3), a similarly good fit as Quebec (Figure 5) is obtained. However, some quarter-diurnal oscillations appear in the predicted ebb discharges, not captured in the observations. These may be due to artifacts from the interpolation functions of the 1D tidal harmonic model, which might appear with constituents of higher frequency (shorter wavelength) when the distance separating the stations becomes close to half the constituent wavelength (cf. Discussion in *Matte et al., 2014b*). At Portneuf (Figure S4), peak flood discharges are underestimated by  $5300 \text{ m}^3\text{s}^{-1}$ , which represents 17.4 % of the diurnal tidal discharge range (cf. Table 4). This can be due to the influence of channel curvature on lateral

water levels (neither accounted for in the 1D model, nor in the 2D projection), or to the negative bias in predicted water levels during the measured period, especially at HW. Moving past the Richelieu rapids to Grondines (Figure S6), the observed water levels are slightly more distorted than the predicted levels (with earlier HW and later LW). This yields slightly time-shifted flood discharges, but the tidal discharge range remains accurately predicted. In Figure S7, a negative bias in predicted water levels of ~20 cm is observed at Batiscan, which is within the prediction accuracy of the nonstationary tidal harmonic model (<30 cm) (Matte *et al.*, 2014b). This results in slightly underestimated and time-shifted flood discharges, whereas ebb discharges are well reproduced. At Bécancour (Figure S8), a positive bias in the predicted tidal signal is obtained along with a less pronounced asymmetry. As a result, the predicted tidal discharges present a larger variability than observed, with lower and time-shifted flood discharges. The measured discharge time series at Trois-Rivières (Figure S9) is very short, which makes it hard to assess the quality of the estimates at this location. With a negative bias in water levels of less than 10 cm (for a tidal range varying between 10-20 cm during the observed period), the discharges are slightly overestimated, but the impact on tidal discharge range cannot be evaluated.

## 4.2 One-Year Tidal Discharge Reconstructions

### 4.2.1 Wetted Surface Areas

Plots of the cumulative wetted surface area for each transect are presented in Figure 7 for the 2007-2008 period. The inundated area (or, equivalently, the integration domain) varies both longitudinally and in time as a function of river discharge and local tidal range (cf. Figure 2). At low discharges, the wetted surface area considerably reduces, mainly due to the presence of a fluvial lake upstream, characterized by an extensive floodplain. This surface is progressively augmented moving downstream and generally increases with MWL during high discharge events, due to the flooding of intertidal flats. The wetted surface area also exhibit semidiurnal variations that follow the amplitude of the tide. The latter varies with river flow, so that semidiurnal fluctuations in wetted surface area are generally stronger during periods of low discharge. Furthermore, fortnightly and monthly variations in tidal range translate into variations in wetted areas with the same periodicity. However, these fluctuations tend to diminish past a certain discharge value. Reasons for this reduction may include the attenuation of the low-frequency tides with discharge, but most likely arise mainly from the presence of steeper topography in the intertidal zone above a certain level (e.g., due to bank enrockment).

Differences between the maximum and minimum wetted surface areas at a given location give some indication of – but do not exactly correspond to – the total extent of intertidal flats upstream. In fact, because of the time lags associated with the landward propagation of the tide, shallow areas are not flooded or dried synchronously throughout the system.

### 4.2.2 Tidal Discharges

Time series of reconstructed tidal discharges are presented in Figures 8 and 9 at Québec (rkm 106.5) and Grondines (rkm 179.5) for the 2007-2008 period. Tidal discharges at Québec (Figure 8) show a large semidiurnal variability. Ebb (positive) discharges are about five times the daily average (in red) during spring tides, exceeding  $50\,000\text{ m}^3\text{s}^{-1}$  under average flow conditions. During neap tides, ebb tidal discharges are slightly below  $40\,000\text{ m}^3\text{s}^{-1}$ . Flood (negative) discharges are overall stronger than ebb discharges during spring tide, reaching almost  $-60\,000\text{ m}^3\text{s}^{-1}$  under average flow conditions. During neap tides, however, they are significantly more

reduced than ebb discharges, with values nearly as low as  $-20\,000\text{ m}^3\text{s}^{-1}$ . Ebb discharges overall last longer than flood discharges, with ebb volumes approximately twice as large as the flood volumes on average, thus yielding a net seaward outflow.

Seasonal variations also appear in the reconstructed signal at Québec as a function of the river flow. During high flow conditions, the strength and duration of ebb (flood) discharges are increased (reduced). Ebb tidal flows can exceed  $60\,000\text{ m}^3\text{s}^{-1}$ , representing more than twice the daily net outflow. When conditions of very high flow and neap tides are combined, near zero and very short flood discharges may occur, as observed at the end of April 2008, meaning that there is no current reversals occurring beyond Québec. While the upstream limit of current reversals is generally located between Grondines (rkm 179.5) and Bécancour (rkm 217) (Matte *et al.*, 2017b), under extreme conditions this limit can be displaced much further seaward (some 60 rkm downstream of Grondines in this case).

Tidal discharges at Grondines (rkm 179.5) are presented in Figure 9. This station is located past the Richelieu rapids in the transition zone between the tidal and tidal-fluvial reaches of the SLFE (Matte *et al.*, 2014b). The influence of the upstream river discharge on tidal discharge variability is drastically increased, compared to the signal at Québec; tidal amplitudes are reduced and tidal asymmetry is enhanced. This results in dynamical changes in the ebb-flood characteristics. Globally, ebb tides last longer than flood tides and the increase in water levels is much shorter and abrupt during flood tides than at downstream locations. Departure of flood discharges from the net average flow is therefore much more important than ebb discharges, but occurs on a shorter time period. During very low discharges (September 2007), current reversals take place during both spring and neap tides, although only during the lowest low water (LLW) in the latter case, because of the diurnal inequality in tidal ranges. During high discharges (January and April 2008), the amplitude of the variations in tidal discharge is significantly reduced, following the decrease in tidal range. While the range of variability approximates  $25\,000\text{ m}^3\text{s}^{-1}$  in periods of low discharge, they barely exceed  $5\,000\text{ m}^3\text{s}^{-1}$  at high discharge. Furthermore, when the mean flow reaches about  $15\,000\text{ m}^3\text{s}^{-1}$ , no more current reversals are observed, even during spring tides, although velocities still experience a significant reduction with the rising tide.

These results highlight the capacity of the model to capture tidal discharge variability under contrasting tidal-fluvial conditions along the river, for a wide range of temporal scales, including intratidal, fortnightly and seasonal. Important tidal flow characteristics are represented by these estimates, such as the times of slack water, maximum ebb and flood discharges, the diurnal inequality in tidal discharges, neap-spring storage effects, and the displacement of the upstream limit of current reversals as a function of river flow and tidal range.

#### 4.2.3 Error Analysis

To evaluate the significance of the tidal discharge reconstructions, error sources were identified and an error analysis was performed based on Eq. (9). From the validation of Morse's estimates of drainage areas (cf. section 3.2.2, Boudreau and Fortin, 2018), an error of  $100\text{ m}^3\text{s}^{-1}$  was attributed to upstream and lateral inflows ( $Q_r$ ) for tributaries between Lasalle and Trois-Rivières. Because no comparison was made between Morse's calculations and the updated (2017) formulas downstream of Trois-Rivières, this estimate was simply doubled to  $200\text{ m}^3\text{s}^{-1}$  to include potential biases downstream as well as random errors from the stage-discharge relations used. Imperfect conceptual representation of the watersheds hydrology may also contribute to the

overall inaccuracy, but the lack of validation data in the St. Lawrence River prevents us from further quantifying the error in the reconstituted discharge time series for tributaries.

Despite the advantages of using a 1D tidal harmonic model to represent water levels rather than direct observations (see next section), such a strategy comes at the price of added errors in the tidal discharge estimates that arise from model uncertainties. These are partly associated with the model underlying assumptions and approximations (cf. Appendix B), and partly due to interpolation errors of the tidal constituent properties. Resulting uncertainties in predicted water levels translate into volume errors and temporal offsets of the predicted occurrence of current reversals. The synchronicity of the tidal discharges may also be affected by errors in tidal asymmetry.

Random errors associated with tidal measurements contribute to the uncertainty in tidal estimates at the analysis stations and were quantified using the correlated noise model implemented in NS\_TIDE (Matte *et al.*, 2013). For the analysed period (1999-2009), these errors translated into RMSE in water levels varying between 0.15 and 0.29 m at the analysis stations. Errors due to spatial interpolation of the tidal coefficients were estimated to vary between 0.11 and 0.30 m, which is comparable to the analysis error. These errors result in RMSE in tidal range varying between 0.02 and 0.44 m (maximum at Saint-Nicolas (rim 124)) and in RMSE in MWL ranging between 0.11 and 0.25 m (maximum at Cap-Santé (rkm 157)), depending on the station (Matte *et al.*, 2014b). In comparison, the dynamic range in water levels varies approximately from 3.5 m upstream (Trois-Rivières) to 6 m downstream (Québec), considering the combined effects of tides and river flow. For use in Eq. (9), mean values of 0.15 and 3 m were used for  $\delta R$  and  $R$ , respectively, representing an estimate of the average longitudinal variability in these parameters. MWL biases, on the other hand, only affect the wetted superficies and were estimated to be approximately 0.16 m on average.

Additional errors also include unresolved phenomena by the tidal harmonic model, which may not fully resolve the nonstationary tidal content. More particularly, the harmonic model has never been tested under very nonstationary conditions (e.g., rapid flood); its performance in such a context thus remains to be assessed. Furthermore, the model does not account for the effects of winds and storm surges. Winds are especially important in Lake Saint-Pierre and may significantly affect the storage volumes. Also, in many estuaries, storm surges can have a “tide-like” signal and they thus add energy in the tidal frequency band as well as at the low frequency end of the spectrum. In its current form, the accuracy of the model is therefore best during non-storm conditions and during periods of weak to moderate non-stationarity. Inclusion of these phenomena should be carried out in the future, either by directly incorporating these variables in the model basis functions (Eq. (6)) or by using more sophisticated functions to spatially interpolate the tidal constituents and residual (unresolved tidal or non-tidal) water levels (e.g., Hess, 2003; Shi *et al.*, 2013).

Lateral variations in water levels in the vicinity of river bends can also yield increased errors in tidal discharge estimates (e.g., Portneuf; Table 4), as they are not accounted for by the 1D model. These lateral water level gradients can be considerable in meandering rivers of high sinuosity (Hidayat *et al.*, 2011) as well as between the channel and floodplains (Jay *et al.*, 2016; Jay *et al.*, 2015; Matte *et al.*, 2017b). (Matte *et al.*, 2017b) investigated lateral variability in the SLFE using a 2D hydrodynamic model, corroborated by field measurements at a series of transects (Matte *et al.*, 2014a). They showed that, in some cross-sections where tidal flats represent a significant percentage of the total river width (e.g. Deschambault, Grondines), the

water levels were nearly the same between the channel and floodplain at HW, whereas the largest lateral gradients were observed near LW (approximately  $\sim 0.1$  m). Interestingly, while near-LW lateral gradients are the largest, this does not coincide with the largest  $dh/dt$  (which typically occurs on early ebb or early flood). Overall, the most significant lateral gradients were observable during the falling tide (ebb), as the tidal flats were emptying into the channel, whereas virtually no lateral gradients were observed during the rising tide (flood). As a result of this asymmetric behavior, most of the error is biased towards LW and does not average out over a tidal cycle.

In this method, the use of a 2D geometry is crucial in adequately representing the wetting-drying of the integration surface for the computation of accurate tidal volumes. Topographic errors associated with imprecision in the raw data, vertical datum, dynamic morphology and the chosen spatial discretization (i.e. finite elements) therefore represent additional sources of uncertainty. Moreover, natural and anthropogenic changes in river morphology should be accounted for if long-term historical reconstructions are envisaged, since historic floodplain bathymetry is often very different from modern bathymetry. In the present application, LIDAR data have an expected accuracy of 0.15 m, but the other sources of topographic inaccuracies are hard to quantify. A combined vertical error of 0.2 m therefore seemed to be a reasonable estimate for the floodplains, averaged over the entire domain.

In sum, systematic errors in water levels and topography, although they virtually have no effect on the time derivative of  $h$  (cf. Eq.(5)), may significantly affect the computed wetted superficies. By combining the estimated biases in MWL (0.16 m), lateral slopes (0.1 m) and topography (0.2 m), we arrive at an estimate of the vertical error  $\delta z$  of 0.46 m. By inspection of Figure 7, it is possible to estimate the average error in wetted surface area from the calculated vertical bias, as follows. Under average discharge conditions, i.e.  $Q_r \sim 12\,000\text{ m}^3\text{s}^{-1}$  at Québec (e.g., in February 2008; Figure 2), the cumulative wetted surface area  $\Omega$  at Québec amounts to approximately  $800\text{ km}^2$ , with a range of variability  $|\Omega|$  over the semi-diurnal tidal cycle of about  $40\text{ km}^2$  (Figure 7). Assuming that the error ratios of wetted surface area to vertical bias, i.e.  $\delta\Omega/\delta z$ , are comparable to the range ratios of wetted surface area to tidal range, i.e.  $|\Omega|/R$ , the uncertainty in wetted surface area can be approximated as:  $\delta\Omega \sim \frac{|\Omega|}{R} \delta z$ . This yields an error estimate for  $\delta\Omega$  of  $6.13 \times 10^6\text{ m}^2$ .

Under mean discharge and tidal range conditions, the amplitude over a tidal cycle of the summed elemental discharges,  $\left| \sum_e Q^e \right|$ , is approximately  $45\,000\text{ m}^3\text{s}^{-1}$  (Figure 8). Solving Eq. (9) using the uncertainty estimates provided above (summarized in Table 5), the tidally-averaged error in computed discharges is estimated to equal  $2285\text{ m}^3\text{s}^{-1}$ . This corresponds to a relative error of 2.5% of the average tidal discharge range at Québec ( $\sim 90\,000\text{ m}^3\text{s}^{-1}$ ), which is comparable to validation results obtained at the Québec cross-section between predicted and ADCP-derived discharges (cf. Table 4).

In the present calculation, the error is dominated by uncertainties in tidal ranges by one order of magnitude compared to errors in the river discharges and wetted surface areas. Uncertainty in tidal ranges is mostly driven by the tidal harmonic model. Under high flow conditions, however, the contribution of the river discharge uncertainty may become of equal

importance to the tidal range error, as suggested by the revised estimates of drainage areas (cf. section 3.2.2, *Boudreau and Fortin*, 2018).

#### 4.3 Benefits and Limitations of the Method

Although it does not capture lateral gradients, benefits of using a 1D tidal harmonic model to represent water levels include the ability to fill temporal gaps in the data (e.g., top panel of Figure 6), to spatially interpolate tidal coefficients between stations, to carry information about the physics and to make tidal discharge forecasts. The descriptive and predictive capabilities of the tidal harmonic model are therefore passed on to the reconstructed tidal discharges, so that they can be estimated under virtually any river discharge ( $Q_r$ ) and ocean tidal range ( $R$ ) conditions. Furthermore, the availability of long tidal records at various locations within estuaries provides the opportunity to reconstruct long and continuous past flow records from historic water level data, provided that sufficient information on the historic evolution of floodplain bathymetry is available. Compared to direct measurements, these cubature computations can be performed at any river sections, as opposed to the installation of fixed apparatus (e.g., H-ADCP), usually limited in number. They can also be used to evaluate flows during flood conditions, when discharges exceed by far the calibration range of both H-ADCPs and traditional rating curves, or in cases of instrument failure. Moreover, this method could potentially be used to improve flow estimates in deltas, such as the NDOI estimate made in San Francisco Bay.

With a 2D discretization of the domain, serving as a descriptor of the river geometry, these components both represent added complexity to a generally simple method. It requires accurate estimations of the upstream freshwater discharge, a sufficient number of tide gauges to allow spatial interpolation of the tidal properties and detailed topographic data over shallow intertidal areas. In large rivers, however, the availability of such data is becoming more and more common, especially along navigation pathways. While the elaboration of a 2D finite element mesh may be a laborious task, this new implementation of the method of cubature represents a significant simplification over traditional numerical models, as it only involves regression analyses for the determination of harmonic coefficients and resolution of the continuity equation over a discretized domain, with no parameterization of the friction properties. Computing time and sensitivity to bathymetric errors are thus expected to be substantially lower than with full 2D numerical models. On the other hand, lateral slopes may arise from phase lags and amplitude differences of the tidal flows between the channel and floodplains. These are not accounted for by this method, which may become a significant drawback in presence of extensive shallow areas.

### 5 Conclusion

Previous attempts to compute tidal discharges in the SLFE either offered limited accuracy or a too high computational cost for real-time and historical analyses. For instance, the cubature estimations made by *Forrester* (1972) did not account for time variations in the surface and cross-sectional areas with tides and river flow, which significantly affect the total mass balance in presence of tidal flats. Similarly, a large number of numerical models have been developed (see, e.g., *Matte et al.* (2017a) for a review of existing models), but most of them only reproduced qualitatively the main tidal and fluvial characteristics of the SLFE, due to a lack of validation data and imprecise discharge boundary conditions. In comparison, high-resolution

models of higher dimensions (2D, 3D), despite their improved accuracy, are generally not suited for long-term analyses (e.g., *Matte et al.*, 2017a; b).

An adaptation of the method of cubature for the computation of tidal discharges was presented and applied to the SLFE, integrating the continuity equation for discharges at different sections. Tidal heights were spatially interpolated between stations by reconstruction of tidal coefficients from a 1D nonstationary tidal harmonic model, thus filling temporal gaps in the tidal data and allowing information on tidal properties to be passed on to the flow estimations. The 1D longitudinal model was expanded laterally and projected on a 2D finite element mesh in order to compute the time-varying wetted surface area, based on detailed topographic data over intertidal flats. Discharge time series were reconstructed at 9 cross-sections in the SLFE and validated against recent discharge data, reaching rRMSE values below 4 % of the diurnal tidal discharge range at downstream locations and below 9 % upstream, with the exception of two transects with shorter records. On the other hand, the error made based on the ratios of predicted to observed flows amounted to 4.5 % when averaged over all transects. Overall, both the synchronism and variability of the observed data were well reproduced by the model. One-year reconstructions conducted at two cross-sections of the SLFE also showed the potential of the method for dynamical inquiries along the tidal-river continuum. The model was able to reproduce the tidal discharge variability at a wide range of temporal scales and under contrasting tidal-fluvial conditions.

This method provides a new means for efficiently and accurately estimating tidal discharges in estuaries. It can be used to issue short-term forecasts (given that upstream river flow can be predicted with sufficient accuracy), in conjunction with discharge measurement stations or as an alternative to the development of dynamic rating curve models. Furthermore, dynamical insights can be gained from historical reconstructions of tidal discharges, with numerous implications from a water resources management perspective, both in terms of water quality and quantity.

## Appendix A: Derivation of Observed Discharges from Water Level and Velocity Data

Transect data consisting of water level and velocity measurements were obtained in the SLFE by *Matte et al.* (2014a), who devised a procedure to reconstruct continuous and synoptic fields from non-synoptic RTK GPS and ADCP data. These fields are used to compute the observed time-varying discharges and section-averaged tidal currents. The calculation consists of the following steps:

1. The bed elevation  $z_b$  (in m) along each transect is obtained by subtracting the instantaneous ADCP water depths,  $H_{ADCP}$ , from the water levels measured by the RTK GPS,  $h_{RTK}$ :

$$z_b = h_{RTK} - H_{ADCP}; \quad (A1)$$

2. The gridded bathymetry points from each crossing are interpolated in time (yielding  $z_{int}$ ) to account for deviations of the boat from the mean transect line (Figure A1), similarly to the interpolation of velocities (see *Matte et al.*(2014a) for details on the procedure; an example of the interpolated bathymetry field is presented in Figure A2):

$$z_b \xrightarrow{\text{gridding}} z_{grd} \xrightarrow{\text{interpolation}} z_{int}; \quad (A2)$$

3. The reconstructed water depths,  $H_{int}$ , are obtained by subtracting the interpolated bathymetry field,  $z_{int}$ , from the interpolated water level field,  $h_{int}$ :

$$H_{int} = h_{int} - z_{int}; \quad (A3)$$

4. Instantaneous discharges  $Q_{obs}$  are computed for a given time  $t_j$  by summing the  $i^{\text{th}}$  specific discharges across the section:

$$Q_{obs}(t_j) = \sum_i \left( u_{int}(t_j) \times H_{int}(t_j) \right)_i \times \Delta x, \quad (A4)$$

where  $u_{int}$  ( $\text{m s}^{-1}$ ) are the interpolated velocities and  $\Delta x$  (m) is the grid spatial resolution (set to 20 m in the present application);

5. Unmeasured discharges  $Q_{est}$  at time  $t_j$  between the riverbank and the first or last measured or interpolated velocity,  $u_m$ , with corresponding depth  $H_m$ , are either estimated using the ratio interpolation method presented by *Fulford and Sauer* (1986), in the case where bathymetry  $z_{avg}$  at subsection  $i$  is known and averaged from other crossings performed at higher water levels:

$$H_{est} = h_{int} - z_{avg}, \quad (A5a)$$

$$Q_{est}(t_j) = \sum_i \left( u_m(t_j) \times H_{est}(t_j) \times \sqrt{\frac{H_{est}(t_j)}{H_m(t_j)}} \right)_i \times \Delta x, \quad (A5b)$$

or by assuming a triangular discharge area between the riverbank and the first or last measured or estimated (from Eq. A5b) subsection velocity,  $u_{est}$  (*MR Simpson*, 2001):

$$Q_{est}(t_j) = \frac{\sqrt{2}}{4} \times u_{est}(t_j) \times H_{est}(t_j) \times L, \quad (A5c)$$

where  $L$  (m) is the distance to the riverbank.

6. The total discharge is computed as the sum of the observed and estimated discharges:

$$Q_{tot}(t_j) = Q_{obs}(t_j) + Q_{est}(t_j). \quad (A6)$$

Section-averaged currents,  $u_{tot}$ , are obtained by dividing the total discharge  $Q_{tot}$  by the cross-sectional area, as follows:

$$u_{tot}(t_j) = \frac{Q_{tot}(t_j)}{\sum_i H_i(t_j) \times \Delta x}, \quad (A7)$$

where  $H_i = H_{int,i}$  in the measured region and  $H_i = H_{est,i}$  in the unmeasured region.

## Appendix B: Derivation of the 1D Nonstationary Tidal Harmonic Model

River tides are nonstationary and nonlinear by nature (*Guo et al.*, 2015), and arise from interactions of the oceanic tide with channel geometry, bottom friction and river flow. Tidal

heights  $h$  in the deep ocean are typically modeled by the classical harmonic analysis (HA) method as:

$$h(t) = b_{0,0} + \sum_{k=1}^n [b_{1,k} \cos(\sigma_k t) + b_{2,k} \sin(\sigma_k t)] \quad (B1)$$

where  $t$  is time,  $\sigma_k$  are a priori known frequencies,  $n$  is the number of constituents, and  $b_{0,0}$ ,  $b_{1,k}$  and  $b_{2,k}$  are unknown coefficients determined by regression analysis to best fit the observations. To include contributions caused by external forcing (river flow and ocean tides) and nonlinear interactions, a functional representation, derived from a theory of river-tide propagation (Jay, 1991) by Kukulka and Jay (2003a; b) and Jay *et al.* (2011), is embedded directly in the HA basis functions. This formulation is based on the Tschebyschev decomposition of the bed stress of the one-dimensional St. Venant equations (Dronkers, 1964), which is the dominant source of nonlinearities in shallow rivers. It is obtained for the critical convergence regime defined by Jay (1991), in which case tides can be considered as diffusive (LeBlond, 1978). In this regime, tidal and fluvial flows are assumed to be of similar magnitude and channel convergence moderate. Conceptually, the constants  $b_{0,0}$ ,  $b_{1,k}$  and  $b_{2,k}$  in Eq. (B1) are replaced by functions of river flow and greater diurnal tidal range (i.e. the difference between higher high water and lower low water within a day) at a convenient station removed from fluvial influence:

$$b_{l,k}(t) = a_{0,l,k} + a_{1,l,k} Q_r^{p_l}(t) + a_{2,l,k} \frac{R^{q_l}(t)}{Q_r^{r_l}(t)} \quad (B2)$$

where  $Q_r$  is the river flow ( $\text{m}^3\text{s}^{-1}$ );  $R$  is the greater diurnal tidal range (m);  $p$ ,  $q$ ,  $r$  are the exponents for each station and frequency band;  $a_{0,l,k}$ ,  $a_{1,l,k}$ ,  $a_{2,l,k}$  are the model coefficients for each station and frequency;  $k$  is the index for tidal constituents ( $k = 1, n$ );  $l$  is the index for coefficients ( $l = 0, 2$ ). The first term on the right-hand side of Eq. (B2) is primarily determined by the convergence/divergence of the channel cross-section. The second term represents the nonlinear response of tides to river flow, while the last term accounts for the effects of frictional interaction through fortnightly and monthly variations in tidal range. Simplifications made to the Saint-Venant model, yielding to this formulation, are presented in more details in Matte *et al.* (2013; 2014b). In practice, the time-varying channel geometry and variations in the ratio of river flow to tidal currents as a function of upriver distance are absorbed into the model parameters and exponents (Jay *et al.*, 2011). In the present application, however, exponents were set to the theoretical values of Kukulka and Jay (2003a; b), rather than iteratively optimized, to allow comparisons between stations and development of a spatial model. The final form of the model is obtained by distributing Eq. (B2) into Eq. (B1) and replacing the exponents by their theoretical values, thus yielding Eq. (6).

The regression coefficients ( $c_0$ ,  $c_1$ ,  $c_2$ ,  $d_{0,k}$ ,  $d_{1,k}$ , and  $d_{2,k}$ ) in Eq. (6) are determined through IRLS analyses (Holland and Welsch, 1977; Huber, 1996), by minimizing the sum of weighted residuals:

$$E = \sum_{j=1}^m w_j^2 (h_j - y_j)^2 \quad (B3)$$

where  $y$  is the observations,  $m$  is the record length and  $w$  is a weighting function. A spatial 1D model of stage and tidal-fluvial properties is obtained by interpolating the regression coefficients

between the analysis stations. Interpolation is made using piecewise cubic Hermite interpolants (*Fritsch and Carlson, 1980*), which are exact interpolants, continuous up to the first derivatives and do not generate extrema or oscillations.

Amplitudes  $A_k$ ,  $B_k$ , and  $C_k$ , and phases  $\alpha_k$ ,  $\beta_k$ , and  $\gamma_k$  can be defined in terms of the coefficients in Eq. (6), at a given location  $r$  along the river:

$$A_k = \sqrt{(d_{0,k}^{(c)})^2 + (d_{0,k}^{(s)})^2}, \quad (\text{B4a})$$

$$B_k = Q_r(t - \tau_Q) \sqrt{(d_{1,k}^{(c)})^2 + (d_{1,k}^{(s)})^2}, \quad (\text{B4b})$$

$$C_k = \frac{R^2(t - \tau_R)}{Q_r^{1/2}(t - \tau_Q)} \sqrt{(d_{2,k}^{(c)})^2 + (d_{2,k}^{(s)})^2}, \quad (\text{B4c})$$

$$\alpha_k = \arctan(d_{0,k}^{(s)} / d_{0,k}^{(c)}), \quad (\text{B5a})$$

$$\beta_k = \arctan(d_{1,k}^{(s)} / d_{1,k}^{(c)}), \quad (\text{B5b})$$

$$\gamma_k = \arctan(d_{2,k}^{(s)} / d_{2,k}^{(c)}). \quad (\text{B5c})$$

Each tidal component of the tidal-fluvial model can be represented in the form of a time series:

$$Z_k(t) = z_k(t)e^{i\sigma_k t} + z_{-k}(t)e^{-i\sigma_k t} = |z_k(t)|e^{-i\phi_k(t)}e^{i\sigma_k t} + |z_{-k}(t)|e^{i\phi_k(t)}e^{-i\sigma_k t}, \quad (\text{B6})$$

where, in terms of the amplitudes and phases:

$$z_{-k}(t) = z_k^*(t) = \frac{1}{2}(A_k \cos \alpha_k + B_k \cos \beta_k + C_k \cos \gamma_k) + i \frac{1}{2}(A_k \sin \alpha_k + B_k \sin \beta_k + C_k \sin \gamma_k). \quad (\text{B7})$$

The resulting time-dependent amplitudes and phases are respectively given by:

$$|Z_k(t)| = |z_k(t)| + |z_{-k}(t)|, \quad (\text{B8a})$$

$$\phi_k(t) = \arctan[\text{Im}(z_{-k}(t))/\text{Re}(z_{-k}(t))]. \quad (\text{B8b})$$

Details of the method are presented in *Matte et al. (2013; 2014b)*. The model is implemented in the NS\_TIDE Matlab toolbox (*Matte et al., 2013*), based on an adaptation of the T\_TIDE code (*Pawlowicz et al., 2002*) that includes robust statistical fitting methods (*Leffler and Jay, 2009*).

### Appendix C: Finite Element Approximation to the Continuity Equation

In order to compute the time-varying wetted surface area and discharges, the continuity equation (Eq. (5)) is approximated by a 2D finite element solution over a discretized domain  $\Omega$ , composed of three-node triangular elements (T3). The time derivative of  $h$  in Eq. (5) is

represented by an approximation function  $N$  multiplied by the nodal values of  $\frac{\partial h}{\partial t}$ , denoted  $\frac{\partial h_n}{\partial t}$

:

$$\frac{\partial h}{\partial t} = \langle N \rangle \left\{ \frac{\partial h_n}{\partial t} \right\}, \quad (C1a)$$

with:

$$\langle N \rangle = \langle 1 - \xi - \eta \quad \xi \quad \eta \rangle, \quad (C1b)$$

where  $\xi$  and  $\eta$  are coordinates defined in the local, elemental reference system (Dhatt *et al.*, 2005). The elemental discharge,  $Q^e$ , computed on one grid element  $\Omega^e(x,y)$ , is defined in terms of the reference element  $\Omega^{ref}(\xi,\eta)$ , as follows:

$$Q^e = \int_{\Omega^e} \frac{\partial h}{\partial t} dx dy = \int_{\Omega^{ref}} \langle N \rangle \left\{ \frac{\partial h_n}{\partial t} \right\} \det(J) d\xi d\eta, \quad (C2a)$$

with:

$$J = \begin{bmatrix} \frac{\partial x}{\partial \xi} & \frac{\partial y}{\partial \xi} \\ \frac{\partial x}{\partial \eta} & \frac{\partial y}{\partial \eta} \end{bmatrix}, \quad (C2b)$$

$$\det(J) = \frac{\partial x}{\partial \xi} \frac{\partial y}{\partial \eta} - \frac{\partial y}{\partial \xi} \frac{\partial x}{\partial \eta} = (x_2 - x_1)(y_3 - y_1) - (y_2 - y_1)(x_3 - x_1) = 2A, \quad (C2c)$$

where the  $x_i$  and  $y_i$  are nodal coordinates of the real element and  $A$  is the elemental surface area ( $m^2$ ). In terms of the nodal values and coordinates, the elemental discharge is given as:

$$Q^e = \frac{1}{6} \left( \frac{\partial h_1}{\partial t} + \frac{\partial h_2}{\partial t} + \frac{\partial h_3}{\partial t} \right) \times \det(J) \quad (C3)$$

Solution to the integral over  $\Omega$  is given by the sum of all elemental discharges, or  $\sum_e Q^e$ .

### Acknowledgments

Work by Pascal Matte was partly supported by scholarships from the Natural Sciences and Engineering Research Council of Canada and Fonds de recherche du Québec – Nature et technologies. Tide gauge data are available for download on DFO's Canadian Tides and Water Levels Data Archive (<http://www.meds-sdmm.dfo-mpo.gc.ca/isdm-gdsi/twl-mne/index-eng.htm>). The authors wish to thank the two reviewers who provided constructive comments on the manuscript.

## References

- Aquatic Informatics Inc. (2012), Report: Global hydrological monitoring industry trends *Rep.*, 30 pp, Vancouver, B.C.
- Bjerklie, D. M., D. Moller, L. C. Smith, and S. L. Dingman (2005), Estimating discharge in rivers using remotely sensed hydraulic information, *J. Hydrology*, 309(1–4), 191-209, doi:<http://dx.doi.org/10.1016/j.jhydrol.2004.11.022>.
- Bouchard, A., and J. Morin (2000), Reconstitution des débits du fleuve Saint-Laurent entre 1932 et 1998. *Rapport Technique RT-101*, 71 pp, Environnement Canada, Sainte-Foy.
- Boudreau, P. and P. Fortin (2018), Débits d'entrée pour les modèles hydrodynamiques bidimensionnels opérationnels du fleuve Saint-Laurent entre Montréal et Québec. *Rapport technique RT-151*, Service Météorologique du Canada, Section Hydrologie et Écohydraulique, Environnement et Changement climatique Canada, Québec. 55 pp. + annexes.
- Bourgault, D., and V. G. Koutitonsky (1999), Real-time monitoring of the freshwater discharge at the head of the St. Lawrence Estuary, *Atmos. Ocean*, 37(2), 203-220.
- Buschman, F. A., A. J. F. Hoitink, M. van der Vegt, and P. Hoekstra (2009), Subtidal water level variation controlled by river flow and tides, *Water Resour. Res.*, 45(10), W10420, doi:10.1029/2009wr008167.
- Cai, H., H. H. G. Savenije, and C. Jiang (2014), Analytical approach for predicting fresh water discharge in an estuary based on tidal water level observations, *Hydrology and Earth System Sciences*, 18(10), 4153-4168, doi:10.5194/hess-18-4153-2014.
- California Department of Water Resources (2016), On estimating Net Delta Outflow (NDO): Approaches to estimating NDO in the Sacramento-San Joaquin Delta. The Natural Resources Agency, State of California, 41 pp.
- Castaing, P., and G. P. Allen (1981), Mechanisms controlling seaward escape of suspended sediment from the Gironde: A macrotidal estuary in France, *Marine Geology*, 40(1–2), 101-118, doi:[http://dx.doi.org/10.1016/0025-3227\(81\)90045-1](http://dx.doi.org/10.1016/0025-3227(81)90045-1).
- Chant, R. J. (2002), Secondary circulation in a region of flow curvature: Relationship with tidal forcing and river discharge, *J. Geophys. Res.*, 107(C9), 3131, doi:10.1029/2001jc001082.
- Chen, Y.-C., T.-M. Yang, N.-S. Hsu, and T.-M. Kuo (2012), Real-time discharge measurement in tidal streams by an index velocity, *Environ Monit Assess*, 184(10), 6423-6436, doi:10.1007/s10661-011-2430-y.
- Costa, J. E., R. T. Cheng, F. P. Haeni, N. Melcher, K. R. Spicer, E. Hayes, W. Plant, K. Hayes, C. Teague, and D. Barrick (2006), Use of radars to monitor stream discharge by noncontact methods, *Water Resour. Res.*, 42(7), W07422, doi:10.1029/2005wr004430.
- da Silva, J. F., and R. W. Duck (2001), Historical changes of bottom topography and tidal amplitude in the Ria de Aveiro, Portugal - trends for future evolution, *Climate Research*, 18, 17-24.

- Daigle, A., F. Bérubé, N. Bergeron, and P. Matte (2013), A methodology based on Particle image velocimetry for river ice velocity measurement, *Cold Reg. Sci. Technol.*, 89(0), 36-47, doi:<http://dx.doi.org/10.1016/j.coldregions.2013.01.006>.
- Dhatt, G., G. Touzot, and E. Lefrançois (2005), *Méthode des éléments finis - Une présentation*, 601 pp., Hermes - Lavoisier.
- Di Baldassarre, G., and A. Montanari (2009), Uncertainty in river discharge observations: a quantitative analysis, *Hydrology and Earth System Sciences*, 13(6), 913-921, doi:10.5194/hess-13-913-2009.
- Dierckx, P., E. Smets, R. Piessens, and M. Temmerman (1981), A new method of cubature using spline functions, *Ocean Dyn.*, 34(2), 61-79.
- Dohler, G. C. (1961), Current survey, St-Lawrence River, Montréal-Québec, 1960Rep., 58 pp, Can. Hydro. Serv. Dept. of Mines and Technical Surveys, Ottawa.
- Dottori, F., M. L. V. Martina, and E. Todini (2009), A dynamic rating curve approach to indirect discharge measurement, *Hydrology and Earth System Sciences*, 6(1), 859-896, doi:10.5194/hessd-6-859-2009.
- Dronkers, J. J. (1964), *Tidal Computations in Rivers and Coastal Waters*, 518 pp., North-Holland Publishing Company, Amsterdam.
- Durand, M., J. Neal, E. Rodríguez, K. M. Andreadis, L. C. Smith, and Y. Yoon (2014), Estimating reach-averaged discharge for the River Severn from measurements of river water surface elevation and slope, *J. Hydrology*, 511(0), 92-104, doi:<http://dx.doi.org/10.1016/j.jhydrol.2013.12.050>.
- Durnford, D., V. Fortin, G. C. Smith, B. Archambault, D. Deacu, F. Dupont, S. Dyck, Y. Martinez, E. Klyszejko, M. Mackay, L. Liu, P. Pellerin, A. Pietroniro, F. Roy, V. Vu, B. Winter, W. Yu, C. Spence, J. Bruxer, and J. Dickhout (2017), Towards an operational water cycle prediction system for the Great Lakes and St. Lawrence River, *B. Am. Meteorol. Soc.*, in press, doi:10.1175/BAMS-D-16-0155.1.
- Dzwonkowski, B., K. Park, and R. Collini (2015), The coupled estuarine-shelf response of a river-dominated system during the transition from low to high discharge, *J. Geophys. Res.*, n/a-n/a, doi:10.1002/2015jc010714.
- Fettweis, M., M. Sas, and J. Monbaliu (1998), Seasonal, Neap-spring and Tidal Variation of Cohesive Sediment Concentration in the Scheldt Estuary, Belgium, *Estuar. Coast. Shelf Sci.*, 47(1), 21-36, doi:<http://dx.doi.org/10.1006/ecss.1998.0338>.
- Forrester, W. D. (1972), Tidal transports and streams in the St. Lawrence River and estuary, *Int. Hydrogr. Rev.*, 49, 95-108.
- Fritsch, F., and R. Carlson (1980), Monotone piecewise cubic interpolation, *SIAM J. Numer. Anal.*, 17(2), 238-246, doi:10.1137/0717021.
- Fulford, J. M., and V. B. Sauer (1986), Comparison of velocity interpolation methods for computing open-channel discharge, in *Selected papers in the hydrologic sciences*, edited by S. Y. Subitsky, pp. 139-144, U.S. Geological Survey Water Supply Paper 2290.

- Godin, G. (1971), Hydrodynamical studies in the St. Lawrence river *Rep. MS Report No. 18*, 116 pp, Marine Sciences Branch, Department of Energy, Mines and Resources.
- Godin, G. (1985), Modification of river tides by the discharge., *J. Waterw. Port Coast. Ocean Eng.*, 111(2), 257-274.
- Godin, G. (1999), The propagation of tides up rivers with special considerations on the Upper Saint Lawrence River, *Estuar. Coast. Shelf Sci.*, 48(3), 307-324.
- Grünler, S., R. Romeiser, and D. Stammer (2013), Estimation of tidally influenced estuarine river discharge from space using along-track InSAR technology: A model-based feasibility study, *J. Geophys. Res.*, 118(7), 3679-3693, doi:10.1002/jgrc.20269.
- Guerrero, J.-L., I. K. Westerberg, S. Halldin, C.-Y. Xu, and L.-C. Lundin (2012), Temporal variability in stage–discharge relationships, *J. Hydrology*, 446–447, 90-102, doi:<http://dx.doi.org/10.1016/j.jhydrol.2012.04.031>.
- Guo, L., M. van der Wegen, D. A. Jay, P. Matte, Z. B. Wang, D. Roelvink, and Q. He (2015), River-tide dynamics: Exploration of non-stationary and non-linear behavior in the Yangtze River estuary, *J. Geophys. Res.*, in press, doi:10.1002/2014JC010491.
- Hasan, G. M. J., D. S. v. Maren, and C. H. Fatt (2013), Numerical Study on Mixing and Stratification in the Ebb-Dominant Johor Estuary, *Journal of Coastal Research*, 201-215, doi:doi:10.2112/JCOASTRES-D-12-00053.1.
- Healy, D., and F. E. Hicks (2004), Index velocity methods for winter discharge measurement, *Can. J. Civ. Eng.*, 31, 407-419.
- Hess, K. W. (2003), Water level simulation in bays by spatial interpolation of tidal constituents, residual water levels, and datums, *Contin. Shelf Res.*, 23(5), 395-414, doi:[http://dx.doi.org/10.1016/S0278-4343\(03\)00005-0](http://dx.doi.org/10.1016/S0278-4343(03)00005-0).
- Hidayat, H., A. J. F. Hoitink, M. G. Sassi, and P. J. J. F. Torfs (2014), Prediction of discharge in a tidal river using artificial neural networks, *Journal of Hydrologic Engineering*, 19(8), 04014006, doi:doi:10.1061/(ASCE)HE.1943-5584.0000970.
- Hidayat, H., B. Vermeulen, M. G. Sassi, P. J. J. F. Torfs, and A. J. F. Hoitink (2011), Discharge estimation in a backwater affected meandering river, *Hydrology and Earth System Sciences*, 15(8), 2717-2728, doi:10.5194/hess-15-2717-2011.
- Hoitink, A. J. F., F. A. Buschman, and B. Vermeulen (2009), Continuous measurements of discharge from a horizontal acoustic Doppler current profiler in a tidal river, *Water Resour. Res.*, 45(11), W11406, doi:10.1029/2009wr007791.
- Holland, P. W., and R. E. Welsch (1977), Robust regression using iteratively reweighted least-squares, *Commun. Stat.-Theor. M.*, 6(9), 813-827, doi:10.1080/03610927708827533.
- Huber, P. J. (1996), *Robust Statistical Procedures*, 2nd edition ed., 67 pp., CBMS-NSF Regional Conference Series in Applied Mathematics, Society of Industrial and Applied Mathematics, Bayreuth, Germany.

- Jalbert, J., T. Mathevet, and A.-C. Favre (2011), Temporal uncertainty estimation of discharges from rating curves using a variographic analysis, *J. Hydrology*, 397(1–2), 83-92, doi:<http://dx.doi.org/10.1016/j.jhydrol.2010.11.031>.
- Jay, D. A. (1991), Green's law revisited: Tidal long wave propagation in channels with strong topography, *J. Geophys. Res.*, 96(20), 585-598.
- Jay, D. A., A. B. Borde, and H. L. Diefenderfer (2016), Tidal-Fluvial and Estuarine Processes in the Lower Columbia River: II. Water Level Models, Floodplain Wetland Inundation, and System Zones, *Estuaries Coasts*, 1-26, doi:10.1007/s12237-016-0082-4.
- Jay, D. A., and T. Kukulka (2003), Revising the paradigm of tidal analysis – the uses of non-stationary data, *Ocean Dyn.*, 53(3), 110-125.
- Jay, D. A., K. Leffler, and S. Degens (2011), Long-term evolution of Columbia River tides, *J. Waterw. Port Coast. Ocean Eng.*, 137(4), 182-191.
- Jay, D. A., K. Leffler, H. L. Diefenderfer, and A. B. Borde (2015), Tidal-Fluvial and Estuarine Processes in the Lower Columbia River: I. Along-Channel Water Level Variations, Pacific Ocean to Bonneville Dam, *Estuaries Coasts*, 38(2), 415-433, doi:10.1007/s12237-014-9819-0.
- Jay, D. A., and J. D. Smith (1990), Circulation, density distribution and neap-spring transitions in the Columbia River Estuary, *Prog. Oceanogr.*, 25(1-4), 81-112.
- Kitheka, J. U., M. Obiero, and P. Nthenge (2005), River discharge, sediment transport and exchange in the Tana Estuary, Kenya, *Estuar. Coast. Shelf Sci.*, 63(3), 455-468, doi:<http://dx.doi.org/10.1016/j.ecss.2004.11.011>.
- Kukulka, T., and D. A. Jay (2003a), Impacts of Columbia River discharge on salmonid habitat: 1. A nonstationary fluvial tide model, *J. Geophys. Res.*, 108(C9), 3293.
- Kukulka, T., and D. A. Jay (2003b), Impacts of Columbia River discharge on salmonid habitat: 2. Changes in shallow-water habitat, *J. Geophys. Res.*, 108(C9), 3294.
- Le Coz, J., G. Pierrefeu, and A. Paquier (2008), Evaluation of river discharges monitored by a fixed side-looking Doppler profiler, *Water Resour. Res.*, 44, 13, doi:W00d0910.1029/2008wr006967.
- LeBlond, P. H. (1978), On tidal propagation in shallow rivers, *J. Geophys. Res.*, 83(C9), 4717-4721.
- Lefavre, D., A. D'Astous, and P. Matte (2016), Hindcast of water level and flow in the St. Lawrence River over the 2005–2012 period, *Atmos. Ocean*, 54(3), 264-277, doi:10.1080/07055900.2016.1168281.
- Leffler, K. E., and D. A. Jay (2009), Enhancing tidal harmonic analysis: Robust (hybrid  $L^1/L^2$ ) solutions, *Contin. Shelf Res.*, 29(1), 78-88.
- Levesque, V. A., and K. A. Oberg (2012), Computing discharge using the index velocity method *Rep. Techniques and Methods 3-A23*, 162 pp, U.S. Geological Survey.

- Li, M., and L. Zhong (2009), Flood–ebb and spring–neap variations of mixing, stratification and circulation in Chesapeake Bay, *Contin. Shelf Res.*, 29(1), 4-14, doi:<http://dx.doi.org/10.1016/j.csr.2007.06.012>.
- Long, B., D. Bouchard, and J.-P. Dumas (1980), Étude des variations de la charge solide du fleuve Saint-Laurent entre Trois-Rivières et Gentilly. Compte rendu des campagnes de terrain (1978-1979).*Rep.*, Université du Québec à Rimouski, INRS-Océanologie, Rimouski.
- Matte, P., D. A. Jay, and E. D. Zaron (2013), Adaptation of classical tidal harmonic analysis to nonstationary tides, with application to river tides, *J. Atmos. Oceanic Technol.*, 30(3), 569-589, doi:10.1175/jtech-d-12-00016.1.
- Matte, P., Y. Secretan, and J. Morin (2014a), Quantifying lateral and intratidal variability in water level and velocity in a tide-dominated river using combined RTK GPS and ADCP measurements, *Limnol. Oceanogr.: Methods*, 12(5), 281-302.
- Matte, P., Y. Secretan, and J. Morin (2014b), Temporal and spatial variability of tidal-fluvial dynamics in the St. Lawrence fluvial estuary: An application of nonstationary tidal harmonic analysis, *J. Geophys. Res.*, 119, 5724–5744, doi:10.1002/2014JC009791.
- Matte, P., Y. Secretan, and J. Morin (2017a), Hydrodynamic modeling of the St. Lawrence fluvial estuary. I. Model setup, calibration and validation, *J. Waterw. Port Coast. Ocean Eng.*, 143(5), 04017010, doi:10.1061/(ASCE)WW.1943-5460.0000397.
- Matte, P., Y. Secretan, and J. Morin (2017b), Hydrodynamic modeling of the St. Lawrence fluvial estuary. II. Reproduction of spatial and temporal patterns, *J. Waterw. Port Coast. Ocean Eng.*, 143(5), 04017011, doi:10.1061/(ASCE)WW.1943-5460.0000394.
- Moftakhari, H. R., D. A. Jay, and S. A. Talke (2016), Estimating river discharge using multiple-tide gauges distributed along a channel, *J. Geophys. Res.*, n/a-n/a, doi:10.1002/2015jc010983.
- Moftakhari, H. R., D. A. Jay, S. A. Talke, T. Kukulka, and P. D. Bromirski (2013), A novel approach to flow estimation in tidal rivers, *Water Resour. Res.*, 49(8), 4817-4832, doi:10.1002/wrcr.20363.
- Morin, J., and O. Champoux (2006), Integrated modelling of the physical processes and habitats of the St. Lawrence River, in *Water Availability Issues for the St. Lawrence River: An Environmental Synthesis*, edited by A. Talbot, pp. 24-39, Environment Canada, Montreal.
- Morse, B. (1990), St-Lawrence River water-levels study: Application of the ONE-D hydrodynamic model.*Rep.*, Transport Canada, Waterways Development Division, Canadian Coast Guard.
- Muste, M., I. Fujita, and A. Hauet (2008), Large-scale particle image velocimetry for measurements in riverine environments, *Water Resour. Res.*, 44(4), W00D19, doi:10.1029/2008wr006950.
- Muste, M., K. Yu, and M. Spasojevic (2004), Practical aspects of ADCP data use for quantification of mean river flow characteristics; Part I: moving-vessel measurements, *Flow Meas. Instrum.*, 15(1), 1-16.

- Nihei, Y., and A. Kimizu (2008), A new monitoring system for river discharge with horizontal acoustic Doppler current profiler measurements and river flow simulation, *Water Resour. Res.*, 44, W00D20, doi:10.1029/2008wr006970.
- Oberg, K., and D. S. Mueller (2007), Validation of streamflow measurements made with acoustic Doppler current profilers, *J. Hydraul. Eng.-ASCE*, 133(12), 1421-1432, doi:10.1061/(asce)0733-9429(2007)133:12(1421).
- Pavelsky, T. M. (2014), Using width-based rating curves from spatially discontinuous satellite imagery to monitor river discharge, *Hydrol. Processes*, 28(6), 3035-3040, doi:10.1002/hyp.10157.
- Pawlowicz, R., B. Beardsley, and S. Lentz (2002), Classical tidal harmonic analysis including error estimates in MATLAB using T\_TIDE, *Comput. Geosci.*, 28(8), 929-937.
- Pillsbury, G. (1939), *Tidal Hydraulics*, 308 pp.
- Plant, W. J., R. Branch, G. Chatham, C. C. Chickadel, K. Hayes, B. Hayworth, A. Horner-Devine, A. Jessup, D. A. Fong, O. B. Fringer, S. N. Giddings, S. Monismith, and B. Wang (2009), Remotely sensed river surface features compared with modeling and in situ measurements, *J. Geophys. Res.*, 114(C11), C11002, doi:10.1029/2009jc005440.
- Prandle, D. (1971), St. Lawrence River tidal model study – Quebec Harbour study – Results of numerical model tests *Rep. LTR-HY-18*, National Research Council Canada, Canadian Hydraulics Centre.
- Prandle, D. (2004), How tides and river flows determine estuarine bathymetries, *Prog. Oceanogr.*, 61(1), 1-26.
- Prandle, D. (2009), *Estuaries: Dynamics, Mixing, Sedimentation and Morphology*, 248 pp., Cambridge University Press, New York.
- Prandle, D., and N. L. Crookshank (1972), Numerical studies of the St. Lawrence River *Rep. Technical Report*, 104 pp, Division of Mechanical Engineering, Ottawa.
- Rantz, S. E. (1982), Measurement and computation of streamflow: Volume 2. Computation of discharge *Rep.*, U.S. Geological Survey, Washington.
- Ruhl, C. A., and M. R. Simpson (2005), Computation of discharge using the index-velocity method in tidally affected areas *Rep.*, U.S. Geological Survey, Scientific Investigations Report 2005-5004, 31 p.
- Sassi, M. G., A. J. F. Hoitink, B. Vermeulen, and Hidayat (2011), Discharge estimation from H-ADCP measurements in a tidal river subject to sidewall effects and a mobile bed, *Water Resour. Res.*, 47(6), W06504, doi:10.1029/2010wr009972.
- Savenije, H. H. G. (2012), Salinity and tides in alluvial estuaries.
- Shi, L., K. W. Hess, and E. P. Myers (2013), Spatial interpolation of tidal data using a multiple-order harmonic equation for unstructured grids, *International Journal of Geosciences*, 4, 1425-1437.

- Simenstad, C. A., L. F. Small, and C. David McIntire (1990), Consumption processes and food web structure in the Columbia River Estuary, *Prog. Oceanogr.*, 25(1–4), 271-297, doi:[http://dx.doi.org/10.1016/0079-6611\(90\)90010-Y](http://dx.doi.org/10.1016/0079-6611(90)90010-Y).
- Simons, R. D., S. G. Monismith, F. J. Saucier, L. E. Johnson, and G. Winkler (2010), Modelling stratification and baroclinic flow in the estuarine transition zone of the St. Lawrence estuary, *Atmos. Ocean*, 48(2), 132-146, doi:10.3137/oc316.2010.
- Simpson, J. H., J. Brown, J. Matthews, and G. Allen (1990), Tidal straining, density currents, and stirring in the control of estuarine stratification, *Estuaries*, 13(2), 125-132, doi:10.2307/1351581.
- Simpson, M. R. (2001), Discharge measurements using a broad-band acoustic Doppler current profiler *Rep. Open-File Report 01-1*, 134 pp, U.S. Geological Survey, Sacramento, California.
- Supharatid, S. (2003), Application of a neural network model in establishing a stage–discharge relationship for a tidal river, *Hydrol. Processes*, 17(15), 3085-3099, doi:10.1002/hyp.1278.
- Syvitski, J. P. M., C. J. Vörösmarty, A. J. Kettner, and P. Green (2005), Impact of Humans on the Flux of Terrestrial Sediment to the Global Coastal Ocean, *Science*, 308(5720), 376-380, doi:10.1126/science.1109454.
- Wallis, S. G., and D. W. Knight (1984), Calibration studies concerning a one-dimensional numerical tidal model with particular reference to resistance coefficients, *Estuar. Coast. Shelf Sci.*, 19(5), 541-562.
- Xiong, Y., and C. Berger (2010), Chesapeake Bay tidal characteristics, *Journal of Water Resource and Protection*, 2(7), 619-628, doi:10.4236/jwarp.2010.27071.

**Table 1.** Mean relative errors in observed discharges at the measurement transects.

Transect	Relative Error (%)
Saint-Jean	2.14
Château-Richer	5.35
Beauport	14.71
Lauzon	3.07
Québec	4.73
Saint-Nicolas	2.16
Neuville	2.29
Portneuf	4.51
Deschambault	6.31
Grondines	1.76
Batiscan	7.26
Bécancour	2.13
Trois-Rivières	1.71

**Table 2.** List of stations and data sources. Analysis and validation stations are shown in normal and italic text, respectively.

rkm	Station	Source
0	Saint-Joseph-de-la-Rive	DFO
30	<i>Islet-sur-Mer</i>	<i>Pressure sensor</i>
38	<i>Rocher Neptune</i>	<i>DFO</i>
45	<i>Ile-aux-Grues South</i>	<i>Pressure sensor</i>
46	<i>Ile-aux-Grues North</i>	<i>Pressure sensor</i>
54	<i>Banc du Cap Brûlé</i>	<i>DFO</i>
66	Saint-François	DFO
78	<i>Saint-Jean</i>	<i>DFO</i>
97	<i>Beauport</i>	<i>Pressure sensor</i>
100	Lauzon	DFO
104	Saint-Charles River	DFO
106.5	<i>Lévis</i>	<i>Pressure sensor</i>
106.5	<i>Québec</i>	<i>Pressure sensor</i>
115	<i>Québec Bridge</i>	<i>Pressure sensor</i>
124	<i>Saint-Nicolas</i>	<i>Pressure sensor</i>
138	Neuville	DFO
146	<i>Sainte-Croix-Est</i>	<i>Pressure sensor</i>
157	<i>Cap-Santé</i>	<i>Pressure sensor</i>
161	<i>Pointe-Platon</i>	<i>Pressure sensor</i>
163.5	Portneuf	DFO
168	<i>Deschambault</i>	<i>Pressure sensor</i>
179.5	<i>Leclercville</i>	<i>Pressure sensor</i>
179.5	<i>Grondines</i>	<i>Pressure sensor</i>
186	Cap-à-la-Roche	DFO
199	Batiscan	DFO
213	<i>Champlain</i>	<i>Pressure sensor</i>
217	Bécancour	DFO
231	Trois-Rivières	DFO
241	<i>Port Saint-François</i>	<i>DFO</i>
264	Lake Saint-Pierre	DFO
288	Sorel	DFO
302	Lanoraie	DFO

**Table 3.** List of tidal constituents included in the analyses for each tidal band, from diurnal to eight-diurnal (D1 to D8).

Tidal Bands	Constituents
D <sub>1</sub>	$\sigma_1, Q_1, \rho_1, O_1, P_1, K_1, \theta_1, J_1, OO_1$
D <sub>2</sub>	$\varepsilon_1, 2N_2, \mu_2, N_2, v_2, M_2, \lambda_2, L_2, S_2, K_2, MSN_2$
D <sub>3</sub>	$MO_3, SO_3, MK_3$
D <sub>4</sub>	$MN_4, M_4, SN_4, MS_4, MK_4, S_4, SK_4$
D <sub>5</sub>	$2MK_5$
D <sub>6</sub>	$2MN_6, M_6, 2MS_6, 2MK_6, 2SM_6, MSK_6$
D <sub>7</sub>	$3MK_7$
D <sub>8</sub>	$M_8$

**Table 4.** Statistics at the validation transects between observed and predicted discharges, namely the root-mean-square error (RMSE), the maximum absolute error (MaxAE) and the mean amplitude ratio (MAR). Values in parentheses are errors relative to the diurnal tidal discharge range.

rkm	Transect	Length of Record (h)	RMSE (m <sup>3</sup> s <sup>-1</sup> )	MaxAE (m <sup>3</sup> s <sup>-1</sup> )	MAR
106.5	Québec	11.3	2841 (3.6 %)	7293 (9.1 %)	0.950
124	Saint-Nicolas	8.8	3486 (3.7 %)	7023 (7.4 %)	0.997
138	Neuville	9.1	2269 (3.3 %)	5440 (7.9 %)	0.943
163.5	Portneuf	6.7	2360 (7.7 %)	5300 (17.4 %)	0.870
168	Deschambault	10.1	1374 (4.6 %)	2328 (7.8 %)	1.025
179.5	Grondines	8.9	775 (5.5 %)	2204 (15.7 %)	0.993
199	Batiscan	7.6	1371 (8.6 %)	3408 (21.4 %)	0.932
217	Bécancour	5.0	660 (18.5 %)	1025 (28.7 %)	0.957
231	Trois-Rivières	0.8	282 (10.5 %)	306 (11.4 %)	1.024

**Table 5.** Uncertainty estimates for variables used in the computation of the tidally-averaged error in discharges. Values are provided for mean discharge and tidal range conditions.

Variable	Value
$\sum_r (\delta Q_r)$	200 m <sup>3</sup> s <sup>-1</sup>
$\left  \sum_e Q^e \right $	45 000 m <sup>3</sup> s <sup>-1</sup>
$R$	3.0 m
$\delta R$	0.15 m
$\delta h_{\text{MWL}}$	0.16 m
$\delta h_{\text{lateral}}$	0.10 m
$\delta z_{\text{topo}}$	0.20 m
$\delta z = \delta h_{\text{MWL}} + \delta h_{\text{lateral}} + \delta z_{\text{topo}}$	0.46 m
$\Omega$	800 km <sup>2</sup>
$ \Omega $	40 km <sup>2</sup>
$\delta \Omega$	6.13 km <sup>2</sup>

## Figure Captions

**Figure 1.** Map of the St. Lawrence fluvial estuary: (red squares) analysis stations; (blue triangles) validation stations; (light blue diamonds) reference stations for ocean tidal range (Sept-Îles) and river discharge (Lasalle). River kilometers are shown beside each station name.

**Figure 2.** (top) Freshwater discharges at Trois-Rivières and Québec during the 2007-2008 period; (bottom) ocean tidal ranges at Sept-Îles.

**Figure 3.** 2D finite element mesh used for integration, showing truncations at the validation transects (in green).

**Figure 4.** Topography (in m relative to MSL) projected on the 2D finite element mesh, including major tributaries.

**Figure 5.** Validation of the reconstructed discharges at Québec on June 15, 2009: (top) Predicted and measured water levels along with the computed wetted surface areas; (bottom) predicted and measured discharges.

**Figure 6.** Same as Figure 5 at Deschambault on August 20, 2009.

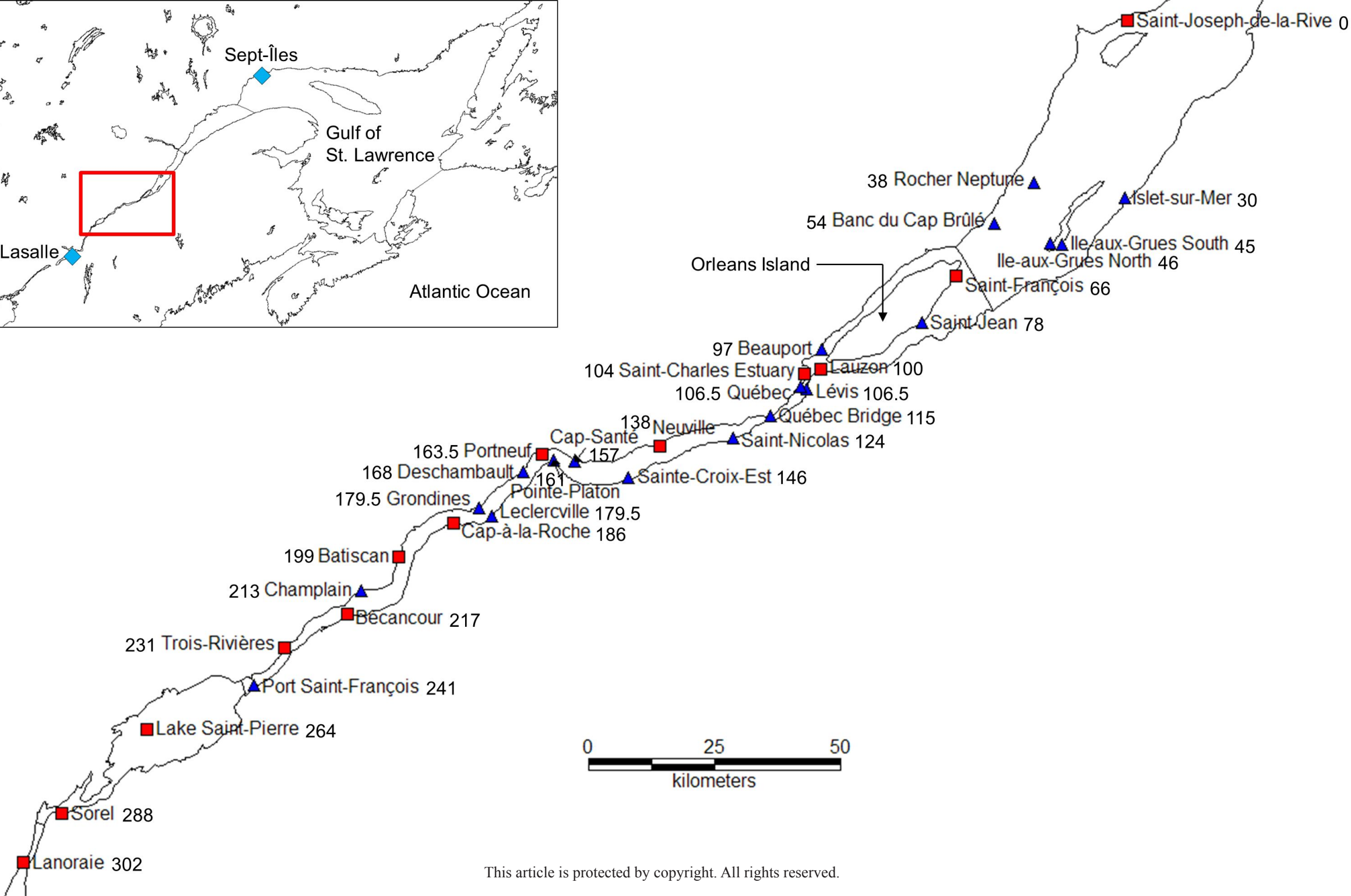
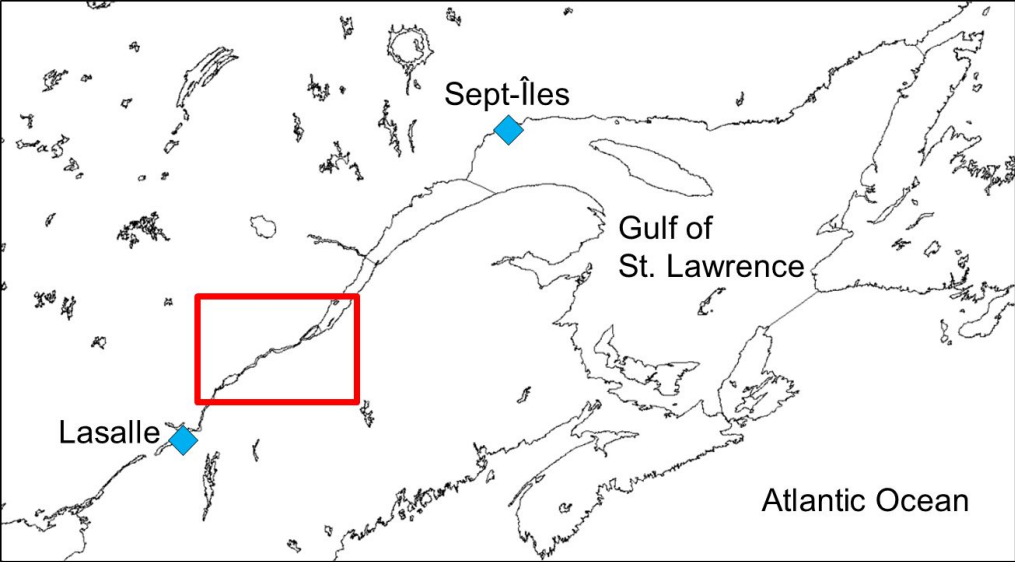
**Figure 7.** Cumulative wetted surface area at the measurement transects during the 2007-2008 period.

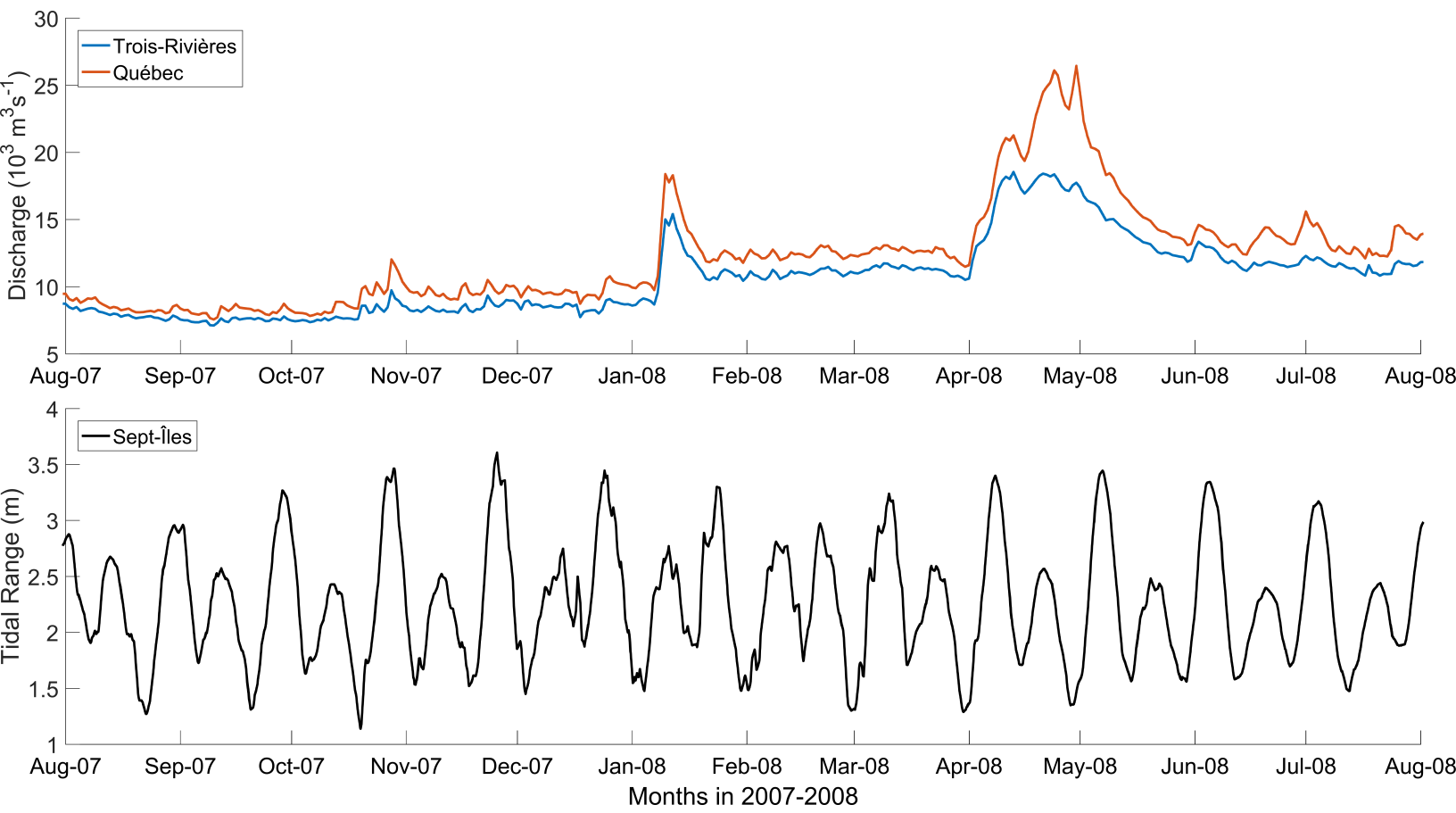
**Figure 8.** Time series of reconstructed discharges at Québec for the 2007-2008 period (blue), along with subtidal freshwater discharges (red).

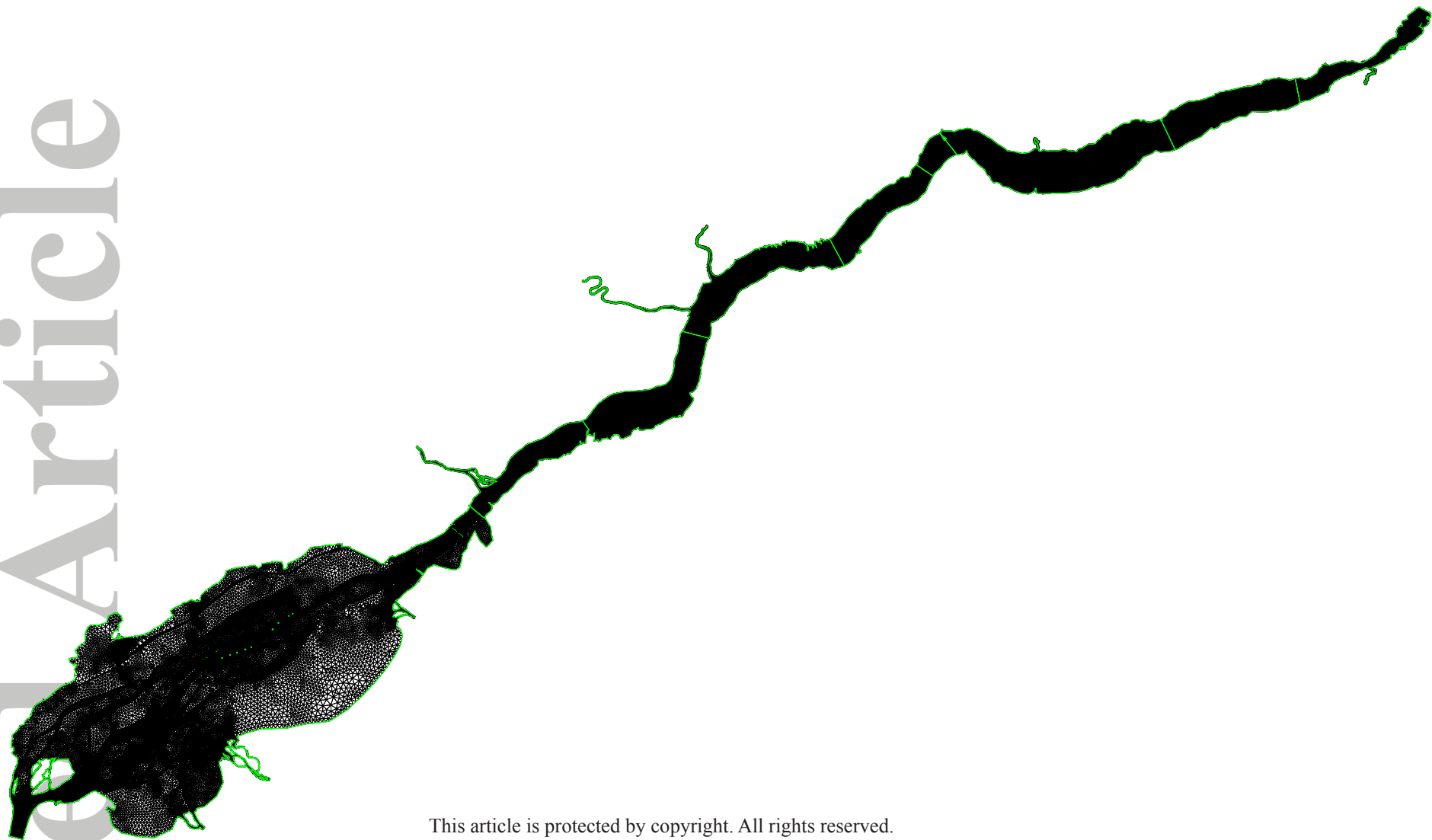
**Figure 9.** Same as Figure 8 at Grondines.

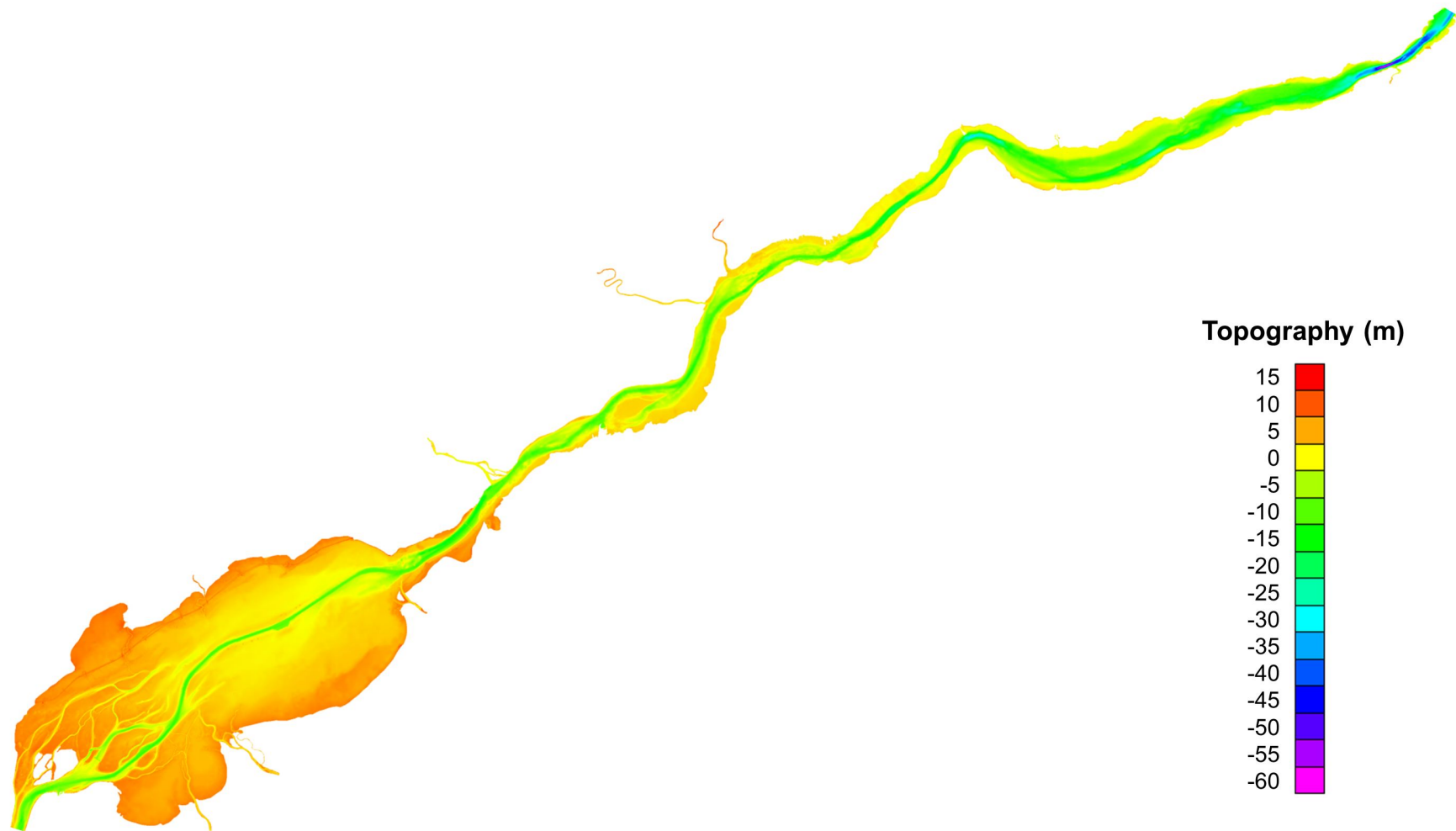
**Figure A1.** Mean transect line (black) fitted through all the crossings made at Batiscan (grey) on June 23, 2009; coordinates are in MTM zone 8.

**Figure A2.** Interpolated bathymetry (in m) in a space-time reference frame, as a function of time (Eastern Daylight Time) and distance from South to North shores. Average cross-channel bathymetry is shown on the left panel.



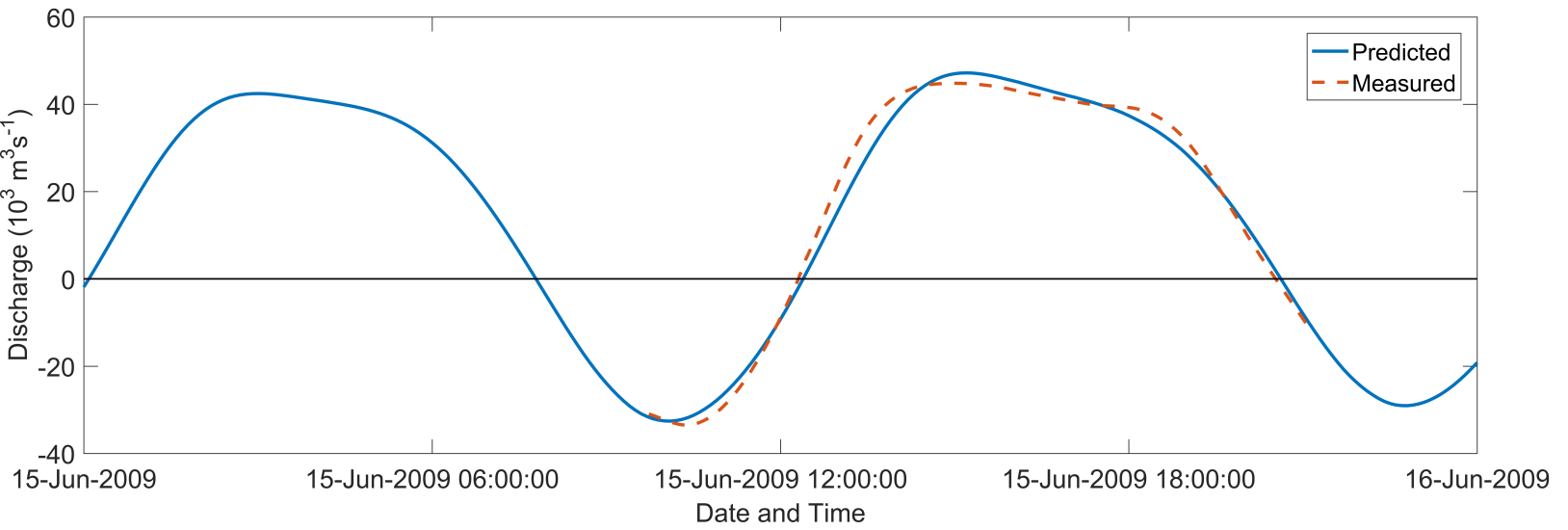
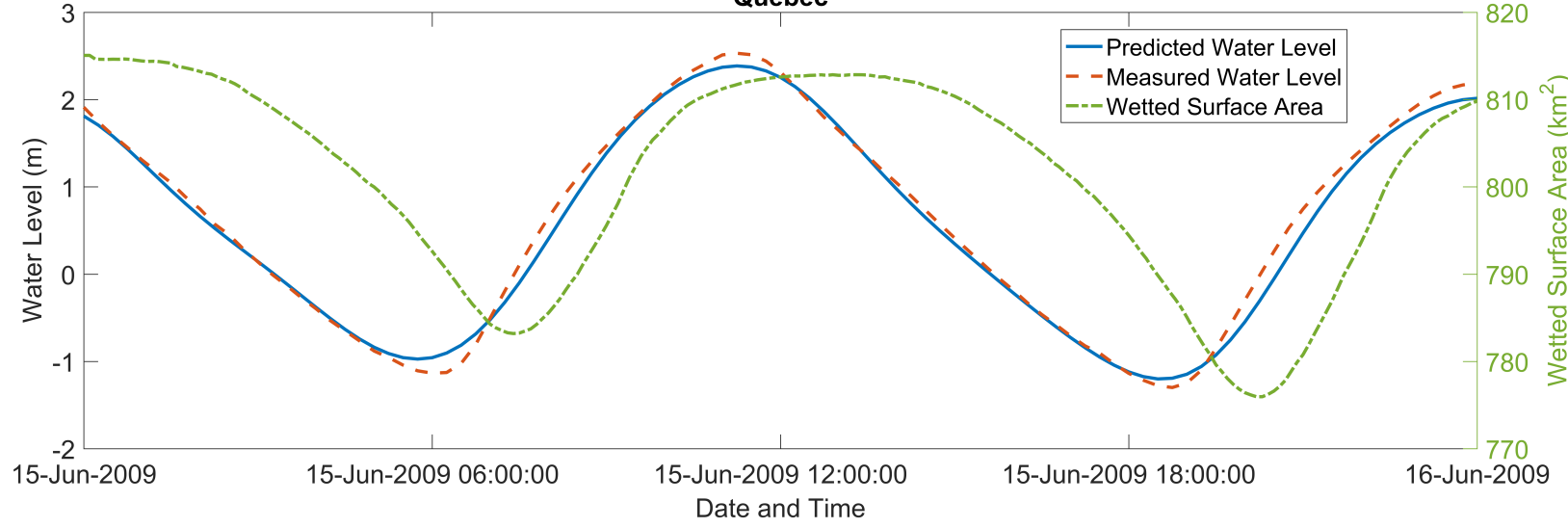






This article is protected by copyright. All rights reserved.

### Québec



### Deschambault

